Can Relaxor Ferroelectric Behavior be Realized for Poly(vinylidene fluoride-*co*-chlorotrifluoroethylene) [P(VDF-CTFE)] Random Copolymers by Inclusion of CTFE Units in PVDF Crystals?

Yanfei Huang,[†,‡,¶] Jia-Zhuang Xu,[†,¶] Thibaut Soulestin,[§] Fabrice Domingues Dos Santos,[§] Ruipeng Li,[#] Masafumi Fukuto,[#] Jun Lei,[†] Gan-Ji Zhong,[†] Zhong-Ming Li,[†] Yue Li,[†,*] and Lei Zhu[‡,*]

[†] *College of Polymer Science and Engineering, State Key Laboratory of Polymer Materials Engineering, Sichuan University, Chengdu 610065, Sichuan, P. R. China*

[‡] *Department of Macromolecular Science and Engineering and Department of Chemistry, Case Western Reserve University, Cleveland, Ohio 44106-7202, United States*

[§] *Piezotech S.A.S., Arkema-CRRA, rue Henri-Moissan, 69493 Cedex Pierre-Benite, France*

[#] *National Synchrotron Light Source II, Brookhaven National Laboratory, Upton, New York 11973, United States*

[¶] These authors contributed equally to the work.

[*] Corresponding authors. Emails: lxz121@case.edu (L. Zhu) and liyue1990liyue@gmail.com (Y. Li).

Abstract

Relaxor ferroelectric (RFE) polymers are attractive for various electrical applications such as electrostrictive actuation, electromechanical sensors, electric energy storage, and electrocaloric cooling because of their high dielectric constants and low hysteresis loss. Current state-of-the-art RFE polymers include poly(vinylidene fluoride-*co*-trifluoroethylene) [P(VDF-TrFE)]-based random copolymers and terpolymers. However, the high costs due to a safety concern of TrFE make their near-term commercialization difficult. It is highly desirable to explore the opportunity of TrFE-free PVDF copolymers [e.g., P(VDF-CTFE); CTFE is chlorotrifluoroethylene] to achieve the RFE behavior by inclusion of CTFE in PVDF crystals (i.e., isomorphism). In this work, two strategies were employed to include CTFE in PVDF crystals. First, high-pressure crystallization was used to obtain extended-chain crystals via the pseudohexagonal paraelectric phase. Structural analyses indicated that CTFE units were largely excluded from the γ unit cells and ferroelectric domains of PVDF, but located as kinks inside the extended-chain lamellae. As a result, no RFE behavior was observed because of large ferroelectric γ domains. The second strategy utilized mechanical stretching at low temperatures (-20 ~ 0 °C) to obtain oriented small β crystallites (ca. 5-7 nm). Structural analyses indicated that CTFE units were excluded from the β unit cells, locating at the crystal-amorphous interfaces. Although the hysteresis loops became somewhat slimmer as a result of small crystallite sizes, the RFE behavior with slim hysteresis loops was still not achieved. This study demonstrated that CTFE units were too large to be included in the tightly packed PVDF unit cells, whether the α, γ, or β phase. In the future, it is desirable to explore other PVDF copolymers with a smaller comonomer such as 1,1-chlorofluoroethylene.

Introduction

Relaxor ferroelectric (RFE) behavior, characterized by a unique nanodomain structure in defective isomorphic crystals,[1-3] is responsible for desirable dielectric properties for polymers, such as high dielectric constants ($\kappa \sim 50$-70, as compared to $\kappa \sim 2$-6 for most linear dielectric polymers[3-5]) and low hysteresis loss in the electric displacement-electric field (D-E) loops. Therefore, RFE polymers are attractive for many potential electrical applications, including electrostrictive actuation,[6-8] electromechanical sensors,[9, 10] electric energy storage,[3, 11, 12] and electrocaloric cooling.[13, 14] The RFE behavior was first discovered for electron beam (e-beam) or γ-ray irradiated poly(vinylidene fluoride-*co*-trifluoroethylene) [P(VDF-TrFE)] random copolymers,[7, 8, 15] and later was extended to P(VDF-TrFE)-based random terpolymers, with the larger termonomer being vinyl chloride (VC), vinylidene chloride (VDC), 1,1-chlorofluoroethylene (CFE), chlorotrifluoroethylene(CTFE), or even hexafluoropropylene (HFP).[16, 17]

It is of great importance to understand the fundamental principles for the RFE behavior in polymers, because it will guide the design and development of new FE polymers with even better electroactive properties and/or performance. Compared to polymers, the RFE behavior has been better understood for ceramics at the atomic to nanoscale levels.[18-20] Owing to the large atomic numbers of inorganic ions in ceramics, high-resolution transmission electron microscopy (TEM) can be used to study the nanodomain structure of RFE ceramics. For example, ordered nanodomains or polar regions (about 2-3 nm) were observed to disperse in the disordered phase of lead manganese niobate [$Pb(Mg_{1/3}Nb_{2/3})O_3$, PMN].[21, 22] As temperature decreases, the conventional paraelectric-to-ferroelectric (PE-FE) Curie transition disappears, because no change in the crystal structure is observed on the mesoscopic scale. Instead, it is replaced by a gradual

change from the true PE phase to the ergodic relaxor phase (i.e., below the Burns temperature, T_B) and then to the nonergodic relaxor phase (i.e., below the freezing temperature, T_f). Between the T_B and the T_f, the dielectric constant exhibits a maximum value with a broad dispersion in the temperature-scan dielectric spectrum. Meanwhile, a slim hysteresis loop is obtained with an ultrahigh dielectric constant (i.e., thousands). Similarly, a genuine relaxor phase is observed for the e-beam irradiated P(VDF-TrFE), where the Curie transition temperature (T_C) disappeared upon heating in differential scanning calorimetry (DSC).[1] However, the dielectric constant shows a broad dispersion peak in the temperature-scan dielectric spectrum, and the D-E loop is slim with a high apparent dielectric constant of 30-50.[1, 7, 8] Although the full molecular-level understanding has not yet been unraveled, on the basis of solid-state ^{19}F nuclear magnetic resonance (NMR) studies,[23, 24] it is speculated that the -CF_3 side groups rearranged from the TrFE units break up large FE domains into nanodomains, and pin the FE switching in the lamellar crystals. Alternatively, a large termonomer can be introduced to P(VDF-TrFE) at a concentration of 5-10 mol.% to induce the gauche (G) conformation[25] and to generate nanodomains.[1, 3] The pinning effect on FE switching can be either weak or strong. In the weak pinning case for P(VDF-TrFE-CFE), nanodomains can transform into transient larger domains at a high enough electric field. Reversible transformation between the transient larger domains and nanodomains leads to a double hysteresis loop (DHL) behavior.[1] In the strong pinning case for P(VDF-TrFE-CTFE), no phase transformation exists and thus a slim single hysteresis loop (SHL) behavior is observed.[3, 26]

For the P(VDF-TrFE-CTFE) terpolymer, the presence of TrFE is important and its content should be above 20 mol.% in order to access the low temperature FE phase for the RFE behavior under the ambient pressure.[27, 28] When the TrFE content is below 20 mol.%, the RFE behavior could not be directly achieved for the sample crystallized from the quiescent melt.[29] We consider

that the P(VDF-TrFE) crystals are tightly packed when the TrFE content is low, and CTFE defects could be largely excluded from the crystalline regions. As a result, large FE domains lead to the normal FE behavior with broad hysteresis loops. Intriguingly, upon mechanical stretching, CTFE units can be pulled into the P(VDF-TrFE) crystals to induce nanodomains and thus the RFE behavior.[29] Later, this phenomenon is also reported for a P(VDF-TrFE-HFP) 58.4/38/3.6 (molar ratio) terpolymer.[30] Upon mechanical stretching, the even larger HFP defects are pulled into the crystalline region of P(VDF-TrFE) to induce the gauche conformation and break up large FE domains into nanodomains. Consequently, the RFE behavior with slim hysteresis loops is achieved with a high dielectric constant of ~45.

However, synthesis of P(VDF-TrFE)-based copolymers and terpolymers requires special facilities (explosion-proof autoclaves) and infrastructures (i.e., on-site production of TrFE monomer) because of the low flash point of TrFE. The high costs of P(VDF-TrFE)-based copolymers and terpolymers make it difficult for near-term commercialization. It is of great interest to search for TrFE-free PVDF-based random copolymers that can also exhibit the RFE behavior.

Recently, commercially available P(VDF-CTFE)[11, 31] [and P(VDF-HFP)[32]] random copolymers were reported to show relatively slim D-E loops with high discharged energy density. Under quiescent melt crystallization conditions, CTFE units should be largely excluded from the crystalline regions of PVDF.[33] However, it is desirable to explore various processing conditions to see if the CTFE units could possibly be included into PVDF crystals and induce the RFE behavior without the presence of TrFE. In this study, P(VDF-CTFE) 95.6/4.4 and 90.5/9.5 (molar ratios) copolymers were synthesized by suspension copolymerization. Note that when the CTFE content is above 15%, P(VDF-CTFE) will become completely amorphous and thus will lose the

FE property. Two strategies were attempted to include CTFE in PVDF crystals. In the first strategy, high-pressure crystallization was performed for both P(VDF-CTFE) samples, and extended-chain crystals with lamellar thicknesses around 60-70 nm were obtained via the pseudohexagonal PE phase under a high pressure of 500 MPa. Structural analyses showed that both samples exhibited the γ phase of neat PVDF at room temperature. It was speculated that CTFE units must be included as kinks inside the extended-chain lamellae. Because of large γ FE domains, these samples exhibited the normal FE behavior with broad hysteresis loops. Apparently, the CTFE kinks were not effective in achieving nanodomains and thus the RFE behavior. The second strategy utilized low-temperature mechanical stretching of quenched P(VDF-CTFE) samples. Small oriented β crystallites (ca. 5-7 nm) with a minor γ phase were obtained. Structural analyses indicated that CTFE units were also excluded from the β/γ unit cells, locating at the crystal-amorphous interfaces. Although narrower hysteresis loops were obtained for the low-temperature stretched samples than the high-pressure crystallized samples, the RFE behavior was still not achieved. From this study, we understand that CTFE is too large to be included inside the unit cells of tightly packed PVDF crystals, whether the α, γ, or β phase. In the future, it is desirable to explore other TrFE-free PVDF copolymers with a smaller comonomer such as CFE to see if the RFE behavior could be achieved for P(VDF-CFE) or not.

Experimental Section

Materials. The P(VDF-CTFE) random copolymers, prepared by suspension polymerization at 48 °C under 80-100 bars, were kindly provided by Piezotech/Arkema (Pierre-Bénite, France). The molar compositions were determined by ^{19}F NMR spectroscopy (see Figure S1 in the Supporting Information). The number-average molecular weight (M_n) and polydispersity

index (PDI) were determined by size-exclusion chromatography (SEC; see Figure S2). For P(VDF-CTFE)-4.4%, M_n = 188 kDa and PDI = 1.82. For P(VDF-CTFE)-9.5%, M_n = 196 kDa and PDI = 1.43.

Suspension Free Radical Copolymerization. Both P(VDF-CTFE) samples were synthesized via suspension free radical copolymerization of vinylidene fluoride (VDF) and CTFE. Here, an example polymerization procedure is given for P(VDF-CTFE)-9.5%. Briefly, VDF (690 g, 8.41 mol) was transferred into a 3 L reactor containing 2052 g of deionized water and a hydroxypropylmethyl cellulose stabilizer at room temperature. The reactor was heated to 48 °C. Then, the free radical initiator was introduced. The pressure inside the reactor was maintained between 80 and 100 bars by injection of a mixture of VDF and CTFE (composition in mol.%: 89/11). After addition of 828 g of the monomer mixture, the polymerization was stopped by fast cooling the reactor to 17 °C. After degassing, the crude product was filtered and the resulting fine white powder was washed 5 times with warm (50 °C) deionized water for 1 h. The final product was dried for 24 h at 60 °C in a ventilated oven (yield = 75 wt.%).

Film Fabrication and Processing. Three types of film samples were fabricated via melt-processing. (1) Quenched samples (Q). The powder sample sandwiched by two aluminum foils was melted at 190 °C for 5 min and hot-pressed at 4000 psi, followed by quenching into liquid nitrogen. The quenched P(VDF-CTFE)-4.4% and P(VDF-CTFE)-9.5% samples are denoted as Q4.4% and Q9.5%, respectively. (2) Quenched and low-temperature stretched (QS) samples. The quenched films were stretched by using a Universal Testing System (Model 5576, Instron, Norwood, MA) at -20 ~ 0 °C. The draw ratio and cross-head speed were 300%-600% and 120-240 mm/min, respectively. The quenched and stretched P(VDF-CTFE)-4.4% and P(VDF-CTFE)-9.5% samples are denoted as QS4.4% and QS9.5%, respectively. (3) High-pressure (HP)

crystallized samples. The quenched and stretched samples were heated above their melting temperatures (T_m, i.e., 160 °C for QS4.4% and 140 °C for QS9.5%) under the ambient pressure for 10 min. Then, a 100 MPa pressure was applied to the sample, and the temperature was continuously increased to 250 °C. After the temperature reached 250 °C, the applied pressure was increased to 500 MPa. The high pressure and high temperature were maintained for 30 min, followed by slow cooling to room temperature before releasing the pressure. The high-pressure crystallized QS4.4% and QS9.5% samples are denoted as HP4.4% and HP9.5%, respectively.

Characterization Methods and Instrumentation. ^{1}H and ^{19}F NMR spectra were recorded using a Bruker NMR spectrometer (500 MHz for ^{1}H and 470 MHz for ^{19}F NMR). The solvent was DMSO-d_6. The molecular weights of P(VDF-CTFE) samples were determined by SEC using a Water 515 HPLC pump and a Waters 2414 differential refractive index (RI) detector. N,N-dimethylformamide (DMF, HPLC grade) was used as the solvent, and the flow rate was 1.0 mL/min. Two Jordi Gel DVB Mixed Bed columns (Jordi Labs, Mansfield, MA) were used and maintained at 40 °C for SEC measurements. Polystyrene standards were used for conventional calibration.

Fourier transform infrared (FTIR) spectra were collected using a Cary 630 FTIR spectrometer (Agilent Technologies, Santa Clara, CA) in an attenuated total reflection (ATR) mode or a Nicolet iS50R FTIR spectrometer (Thermo Fisher Scientific, Waltham, MA) in a transmission mode. The scan resolution was 4 cm^{-1} with a total of 32 scans. A Linkam FTIR600 hot stage (Linkam Scientific Instruments, Tadworth, U.K.) was used to acquire time-resolved FTIR spectra.

DSC was performed on a TA Q2000 differential scanning calorimeter (TA Instruments, New Castle, DE) at a scanning rate of 10 °C/min under a nitrogen flow of 50 mL/min. Specimens

(1~3 mg) were heated from room temperature to 180 °C to study the melting behavior. High-pressure crystallized samples were heated from room temperature to 130 °C for HP4.4% and 150 °C for HP9.5%, followed by cooling to room temperature and then reheating to 180 °C.

The field-emission scanning electron microscopy (FE-SEM, Nova NanoSEM 450, FEI, Hillsboro, OR) was used to visualize the crystal morphology operating at 3 kV, and secondary electron images were recorded. To prepare for SEM observation, the samples were cryogenically fractured in liquid nitrogen, followed by etching with an etching reagent prepared using the method proposed by Vanghan.[34] After washing and drying, a thin layer of gold was sputter-coated on the prepared cross-section to make the sample electrically conductive for SEM observation.

Two-dimensional (2D) small-angle X-ray scattering (SAXS) and wide-angle X-ray diffraction (WAXD) measurements were performed at the 11-BM Complex Materials Scattering (CMS) beamline at the National Synchrotron Light Source II (NSLS-II), Brookhaven National Laboratory (BNL). The X-ray wavelength (λ) was 0.0918 nm. A Pilatus 2M detector (Dectris, Baden-Dättwil, Switzerland) was used for SAXS and an in-vacuum CCD (Photonic Science, St. Etienne de St. Geoirs, Isere, France) detector was used for WAXD experiments. To allow the SAXS signal to pass through, the WAXD detector was shifted and rotated by ~19° from the incident X-ray beam direction. The distances between sample and detectors were 223.3 mm for WAXD and 3000 mm for SAXS, which were calibrated using silver behenate with the first-order reflection at a scattering vector of q = 1.076 nm^{-1}, where $q = (4\pi\sin\theta)/\lambda$ with θ being the half-scattering angle. The data acquisition time for each SAXS and WAXD pattern was 10 s. An Instec HCS402 hot-stage (Instec, Inc., Boulder, CO) was used for precise temperature control. One-dimensional (1D) WAXD curves were obtained by integration of the corresponding 2D WAXD patterns.

D-E loop measurements were performed using a Premiere II ferroelectric tester (Radiant Technologies, Inc., Albuquerque, NM) in combination with a Trek 10/10B-HS high-voltage amplifier (0-10 kV AC, Lockport, NY). The applied voltage had either a bipolar or a unipolar sinusoidal waveform at 10 Hz. Gold (Au) electrodes with an area of 4.52 mm^2 and a thickness around 10 nm were evaporated on both sides of the film sample using a Q300TD sputter coater (Quorum Technologies, Ltd., U.K.). The Au-coated film samples were immersed in silicon oil (Fisher 460-M3001) to avoid corona discharge. A home-built sample fixture was used to connect the electrodes on both sides of the film sample with the interface of the Radiant ferroelectric tester using high-voltage cables.

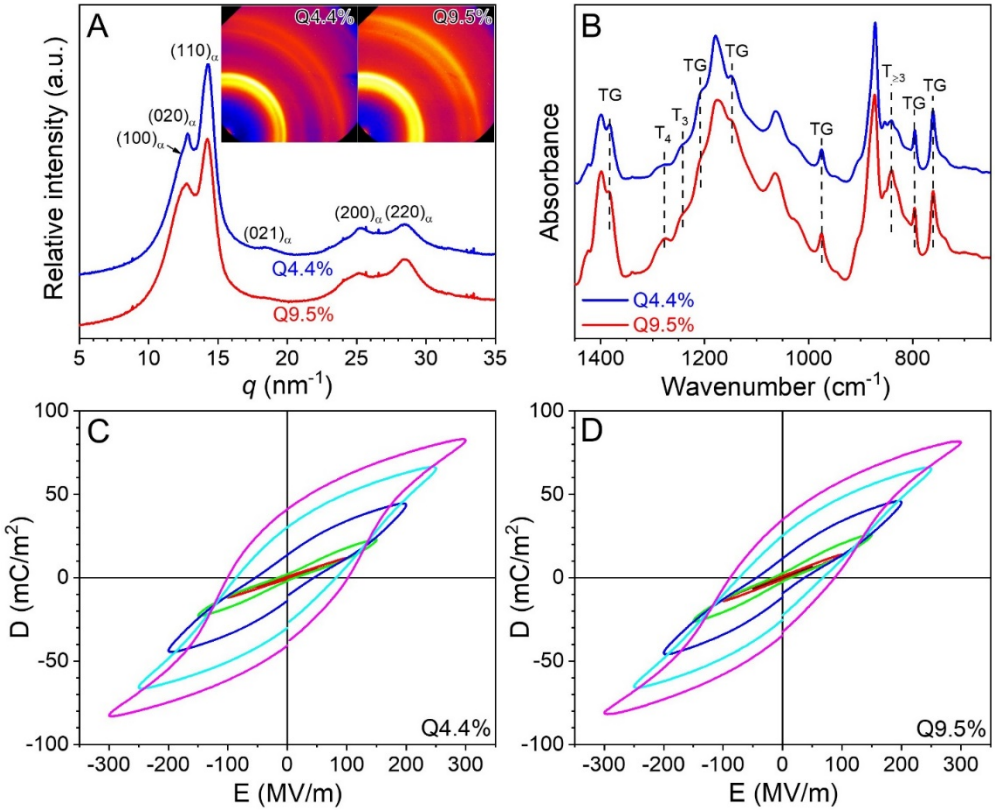

Figure 1. (A) 1D WAXD profiles and corresponding 2D patterns (insets) for Q4.4% and Q9.5% at 25 °C. (B) FTIR spectra for Q4.4% and Q9.5%. The FTIR is in the transmission mode. Bipolar D-E loops are shown for (C) Q4.4% and (D) Q9.5%, respectively. Two loops were recorded at each poling field and the second loop is presented. The poling frequency was 10 Hz with a sinusoidal waveform.

Results and Discussion

Crystalline Structure and Ferroelectric Property of Quenched Samples. The crystalline structures of Q4.4% and Q9.5% were studied by WAXD (Figure 1A). Figure 1A shows the 1D WAXD profiles obtained from the 2D WAXD patterns in the insets. Typical α-form reflections were observed for both samples. From the DSC study, the T_ms were 144 °C and 133 °C and crystallinities were 39 wt.% and 33 wt.% for Q4.4% and Q9.5%, respectively (data not shown). The heat of fusion for the perfect α PVDF crystal was taken as 104.5 J/g.[35] Both WAXD patterns showed a weak orientation, which might be related to the melt flow during hot-pressing. The corresponding 2D SAXS patterns are shown in Figure S3. The lamellar long periods were 7.5 and 7.6 nm for Q4.4% and Q9.5%, respectively. Since WAXD could only provide information of interchain distances and was difficult to differentiate the γ phase from either the α or the β phase, FTIR was used to provide additional information on various chain conformations, such as trans-gauche (TG) in the α phase, TTTG (or T_3) in the γ phase, and all trans ($T_{>3}$) in the β phase. From Figure 1B, absorption bands for the TG conformation in the α phase were seen at 761, 795, 975, 1146, 1209, and 1380 cm^{-1}. The absorption bands for the γ phase were found at 843 and 1240 cm^{-1}, and those for the β phase were observed at 843 and 1276 cm^{-1}, respectively. However, the absorption bands for the γ/β phases were quite weak, indicating that the α phase dominated. The small amounts of γ/β phases could be a result of homogeneous nucleation/fast crystallization when quenching the samples into liquid nitrogen. Note that an extremely high cooling rate, e.g., >2000 K/s, would lead to the formation of β crystals via homogeneous nucleated crystallization.[36, 37]

Figures 1C and D show bipolar D-E loops for the Q4.4% and Q9.5% films at room temperature, respectively. Normal ferroelectric behavior with broad hysteresis loops was observed.

Because the WAXD reflections in Figure 1A fit the α phase well for both samples, we consider that CTFE units should be mostly excluded from the α unit cells because of its large size. The D-E loops for Q9.5% appeared slightly slimmer than those of Q4.4%. This could be attributed to smaller crystallite and ferroelectric domain sizes due to a higher amount of CTFE defects in Q9.5%.

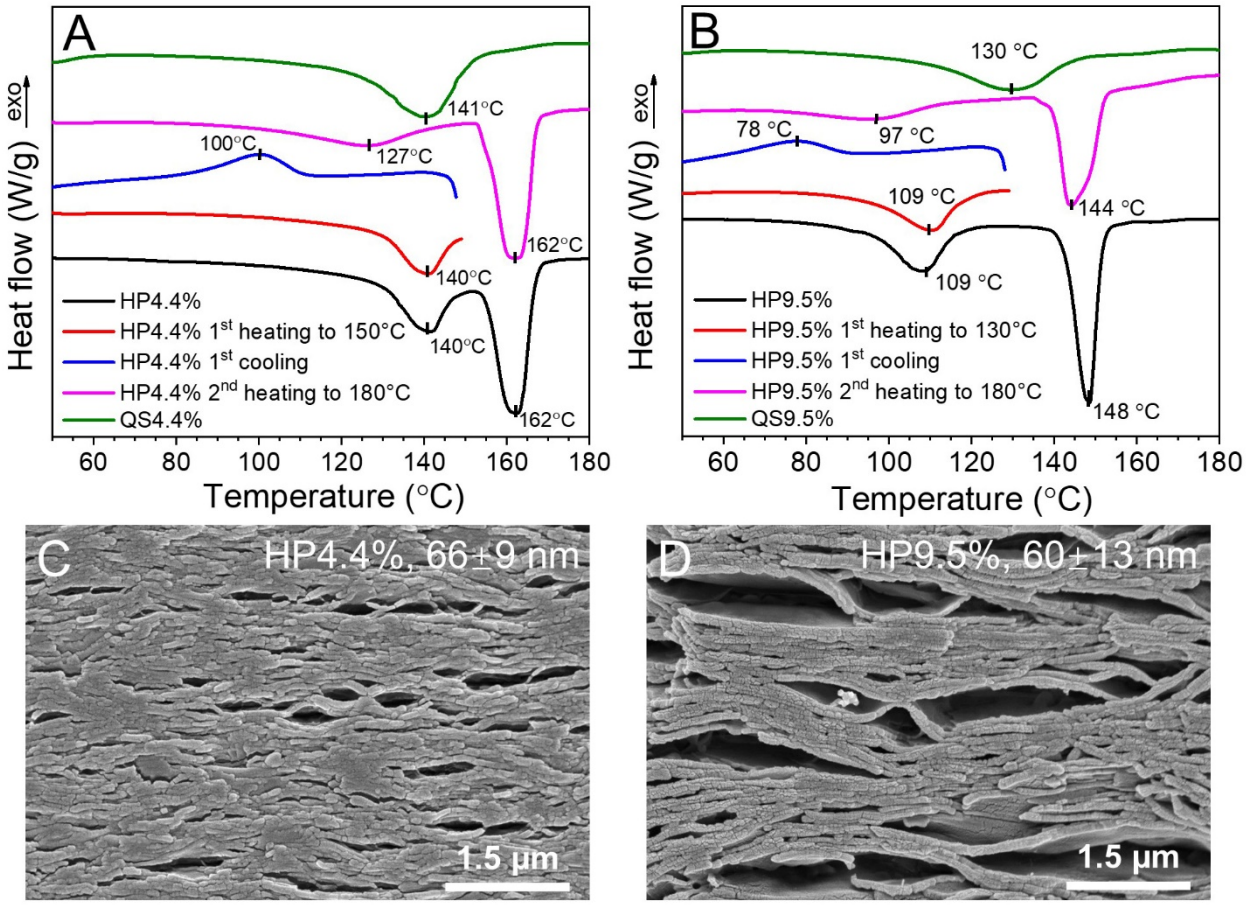

Figure 2. DSC thermograms of (A) HP4.4% and (B) HP9.5% during the first heating, first cooling, and second heating processes in comparison with QS4.4% and QS9.5% samples. SEM images of extended-chain lamellae for (C) HP4.4% and (D) HP9.5%, respectively.

Inclusion of CTFE into PVDF Crystals by High-Pressure Crystallization and the Ferroelectric Properties. One strategy to include CTFE units into PVDF crystals is to crystallize P(VDF-CTFE) under a high pressure. It is known that high-pressure crystallization can access the pseudohexagonal PE phase for PVDF and P(VDF-TrFE) with a low TrFE content (i.e., <20

mol.%).[28] Due to the large interchain distance of the PE phase, we expect that CTFE units can be included into PVDF crystals. Figures 2A,B show DSC thermograms for HP4.4% and HP9.5% samples, in comparison with QS4.4% and QS9.5%. Before high-pressure crystallization, QS4.4% and QS9.5% showed T_ms at 141 and 130 °C, respectively. The lower T_m values than that (~175°C) of the PVDF homopolymer[38] suggested thinner lamellar crystals for the PVDF crystals in P(VDF-CTFE) due to the presence of CTFE defects; the more CTFE defects, the lower the T_m and the crystallinity. After high-pressure crystallization, the T_m increased to 162 and 148 °C for HP4.4% and HP9.5%, respectively. We consider that crystalline lamellae must have increased the thickness due to enhanced chain-sliding via the pseudohexagonal PE phase during high-pressure crystallization. Indeed, FE-SEM showed thick lamellae for cross-section etched HP4.4% (Figure 2C) and HP9.5% (Figure 2D). The average lamellar thicknesses for HP4.4% and HP9.5% were estimated to be 66±9 and 60±13 nm, respectively, remarkably higher than those of conventional PVDF (ca. 10 nm).[34] The lower ECC lamellar thickness for HP9.5% than HP4.4% could be attributed to possible short $(CTFE)_n$ blocks in the P(VDF-CTFE) chains, which were unlikely to be included in the ECCs. Note that the gaps between some lamellae for both samples originated from electron beam damage during the SEM observation. From these studies, we consider that extended-chain crystals were achieved via high-pressure crystallization for P(VDF-CTFE). We speculated that CTFE units should have been included in the extended-chain crystalline lamellae.

In addition to the T_m, another endothermic peak at a lower temperature was observed for each sample, i.e., 140 °C for HP4.4% and 109 °C for HP9.5%. Such a phenomenon was also observed for samples crystallized under other combinations of high pressure (200-500 MPa) and temperature (220-270 °C) (see Figure S4). If the samples were heated to just above the lower endothermic peaks but below the T_m (i.e., 150 °C for HP4.4% and 130 °C for HP9.5%; see the red

curves), followed by subsequent cooling (blue curves) and reheating (magenta curves), certain reversibility was observed (Figures 2A,B). For example, upon second heating, the lower endothermic peaks became broader and shifted to 127 °C for HP4.4% and 97 °C for HP9.5%. The T_m remained at 162 °C for HP4.4% and slightly decreased to 144 °C for HP9.5%. If both samples were directly heated above the T_m for the first heating, the second heating curves were similar to those of the Q4.4% and Q9.5% samples. Basically, the lower endothermic peaks completely disappeared. This was because the extended-chain crystals were melted above T_m, and subsequent crystallization under the ambient pressure resulted in folded-chain crystals.

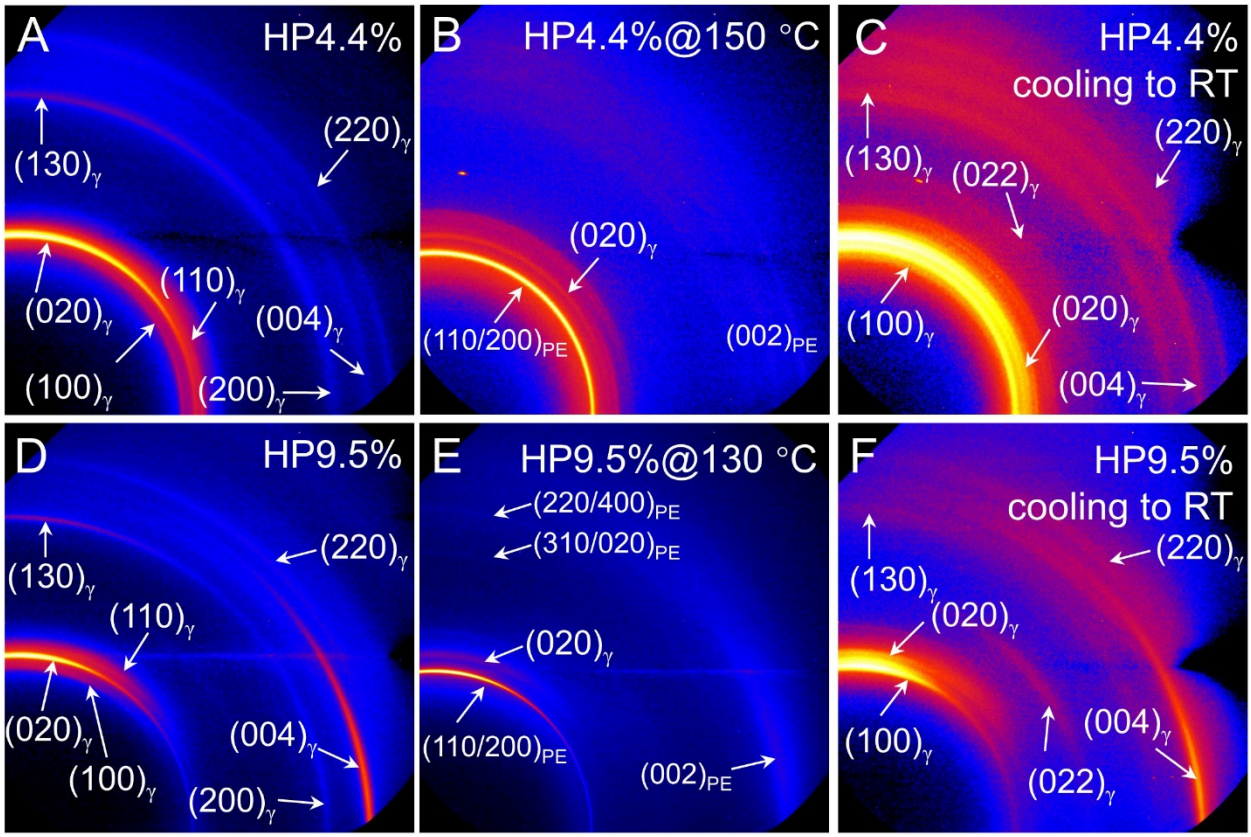

Figure 3. 2D WAXD patterns for (A-C) HP4.4% and (D-F) HP9.5% at (A,D) room temperature, (B) 150 °C for HP4.4% and (E) 130 °C for HP9.5%, and (C,F) cooling back to room temperature. The X-ray beam was directed in the transverse direction to the film samples (see Figure S5 for definition of the transverse direction).

There could be several reasons for the reversible lower endothermic peaks, namely, melting/recrystallization of secondary or different form crystals, or a reversible phase transition. To understand the nature of the lower endothermic peaks, 2D WAXD experiments were performed in the transverse direction of the film samples, and results are shown in Figure 3. The corresponding 2D SAXS patterns are shown in Figure S5. Crystal orientation was preserved (i.e., inherited from the starting QS film samples) after high-pressure crystallization, especially for HP9.5%. The corresponding 1D WAXD profiles for HP4.4% and HP9.5% are shown in Figures 4A and B, respectively. At room temperature, typical reflections for the γ phase were observed, $(100)_\gamma$, $(020)_\gamma$, $(110)_\gamma$, $(130)_\gamma$, $(200)_\gamma$, $(004)_\gamma$, and $(220)_\gamma$, with $(020)_\gamma$ being the strongest reflection. Here, $(100)_\gamma$, $(020)_\gamma$, and $(004)_\gamma$ were used to calculate the unit cell dimensions of the γ crystals by assuming the same monoclinic structure (i.e., $\beta = 92.9°$) as the reported γ phase for neat PVDF:[39] $a = 0.489$ nm, $b = 0.901$ nm, and $c = 0.914$ nm for the HP4.4%, and $a = 0.487$ nm, $b = 0.920$ nm, and $c = 0.918$ nm for the HP9.5%. These unit cell dimensions were somewhat smaller than those of PVDF γ phase reported in the literature ($a = 0.496$ nm, $b = 0.958$ nm, and $c = 0.923$ nm). We speculated that the smaller unit cell dimensions could probably be attributed to the high pressure (i.e., 500 MPa) applied during crystallization, which induced a denser chain packing. The TTTG conformation in γ phases for both HP4.4% and HP9.5% was confirmed by FTIR results at 40 °C in Figures 4C and D. Typical long T_3G or $T_{\geq 3}$ conformation bands were observed at 1430, 1274 (shoulder), 1254 (shoulder), 1234, 836, 812, and 773 cm^{-1}.[40] Judging from both WAXD and FTIR results for HP4.4% and HP9.5%, CTFE units should not be directly included in the γ unit cells, because their dimensions were nearly the same as those for neat PVDF. Given the extended chain crystals for HP4.4% and HP9.5% (see Figure 2), we speculated that CTFE units should be included

in the extended-chain crystals as kinks, similar to the case of the cooled FE phase in P(VDF-TrFE) reported before.[39, 41]

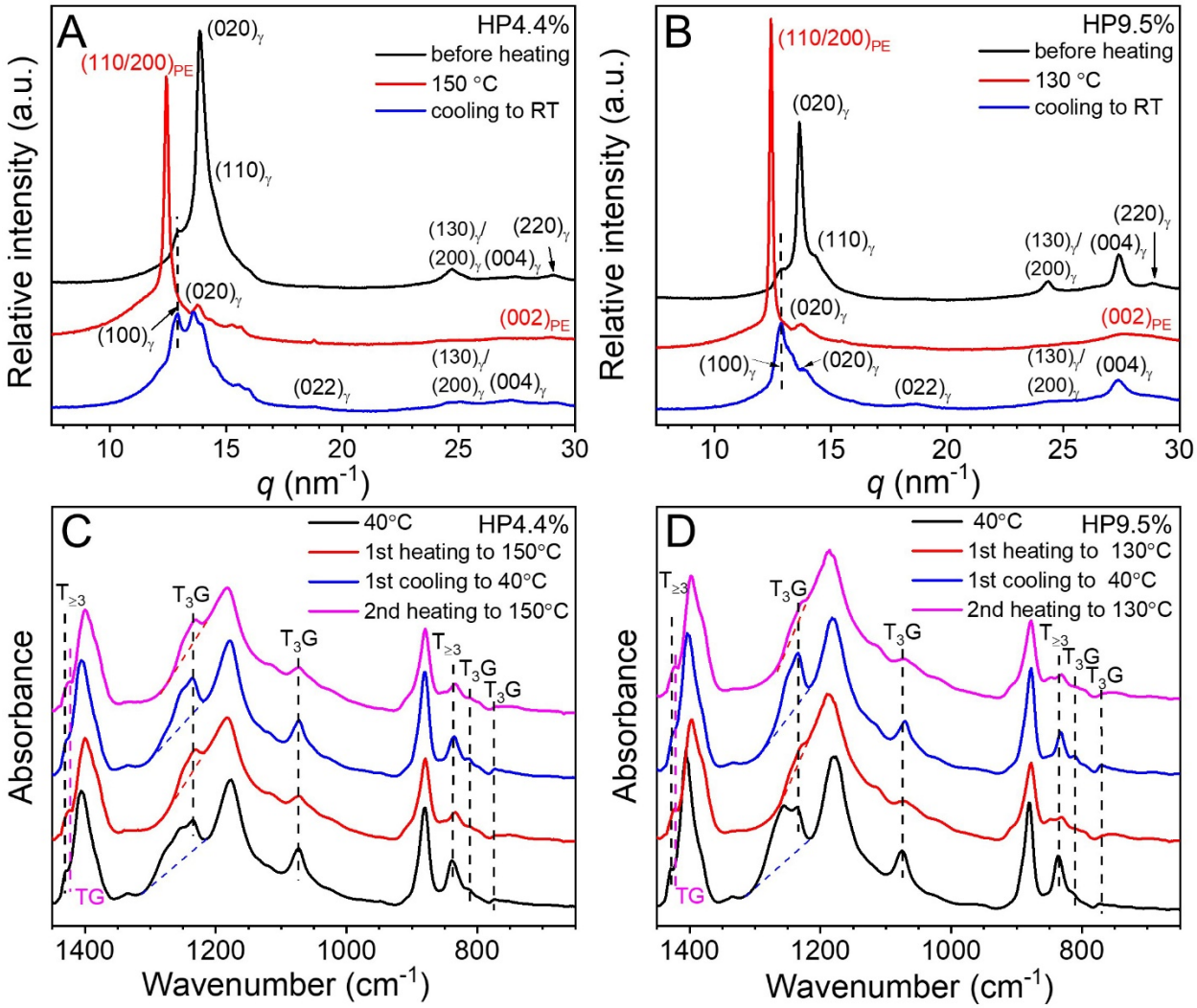

Figure 4. 1D WAXD profiles for (A) HP4.4% and (B) HP9.5% during a thermal treatment process; (i) room temperature, (ii) first heating to 150 °C for HP4.4% and 130 °C for HP9.5%, and (iii) first cooling to room temperature. FTIR spectra for (C) HP4.4% and (D) HP9.5% during a reversible heating and cooling process; (i) 40 °C, (ii) first heating to 150 °C for HP4.4% and 130 °C for HP9.5%, (iii) first cooling to 40 °C, and (iv) second heating to 150 °C for HP4.4% and 130 °C for HP9.5%. FTIR experiments were run in the transmission mode.

Upon heating above the lower endothermic peaks, the 1D WAXD profiles changed dramatically for both samples. Other than certain weak remaining reflections from the γ phase, e.g., $(020)_\gamma$, a sharp reflection was observed at 12.43 nm^{-1} (0.505 nm) and a broad peak was

centered at 27.70 nm^{-1}, respectively. In the 2D WAXD pattern for the HP9.5% at 130 °C (Figure 3E), the 12.43 nm^{-1} reflection was in the vertical direction and the 27.70 nm^{-1} reflection was in the horizontal direction. This 2D WAXD pattern could be explained by the high temperature PE phase, which should be similar to that for P(VDF-TrFE) above the Curie transition temperature (T_C).[39, 41] The sharp peak at 12.43 nm^{-1} was assigned as the $(110/200)_{PE}$ reflection and the broad peak at 27.70 nm^{-1} was assigned as the $(002)_{PE}$ reflection. Meanwhile, weak $(310/020)_{PE}$ and $(220/400)_{PE}$ reflections were seen in Figure 3E, with a *q* ratio to the $(110/200)_{PE}$ reflection of 1: √3: √4, suggesting a pseudohexagonal structure for the PE phase.[26] A similar hexagonal PE phase was also obtained for the HP4.4% at 150 °C (Figures 3B and 4A). Note that the *d*-spacing for the $(110/200)_{PE}$ was 0.505 nm, larger than both *d*-spacings (0.486 nm) for the $(100)_{\gamma}$ reflection for HP4.4% and HP9.5%. After cooling back to room temperature, most γ phase reflections returned although peak intensities dramatically changed for both samples, as compared to the original high-pressure crystallized samples. From these WAXD results, the lower endothermic peak in DSC should be assigned as the Curie transition from the FE γ phase to the pseudohexagonal PE phase. Note that, other than P(VDF-TrFE) and P(VDF-TFE) (TFE is tetrafluoroethylene),[39] no Curie transition has been reported for other PVDF random copolymers, such as P(VDF-CTFE) and P(VDF-HFP), at the ambient pressure. This is the first time that a γ-PE Curie transition was observed for high-pressure crystallized P(VDF-CTFE) random copolymers due to the inclusion of CTFE defects as kinks in the extended-chain crystals.

The reversible γ-PE Curie transition could also be seen in the FTIR spectra for both HP4.4% and HP9.5% samples in Figures 4C and D. The absorption bands at 1274, 1254, 1234, 1075, and 836 cm^{-1} dramatically dropped the intensities or nearly disappeared after heating to 150 °C for HP4.4% and 130 °C for HP9.5%. Meanwhile, a weak peak at 1421 and 855 cm^{-1} for the TG

conformation appeared, indicating the formation of the high temperature PE phase. This PE phase should be similar to the high temperature PE phase in P(VDF-TrFE), which had combined TG and TTTG conformations with high segmental mobility in the crystal. After cooling to 40 °C, these absorption bands for the γ phase returned. Upon second heating, these absorption bands decreased the intensity or disappeared again. However, DSC results in Figures 2A,B and WAXD results in Figures 4A,B suggested that structural changes must have happened by the heating and cooling cycles. We speculated that the CTFE kinks might be gradually kicked out of the extended chain crystals upon thermal annealing above the T_C.

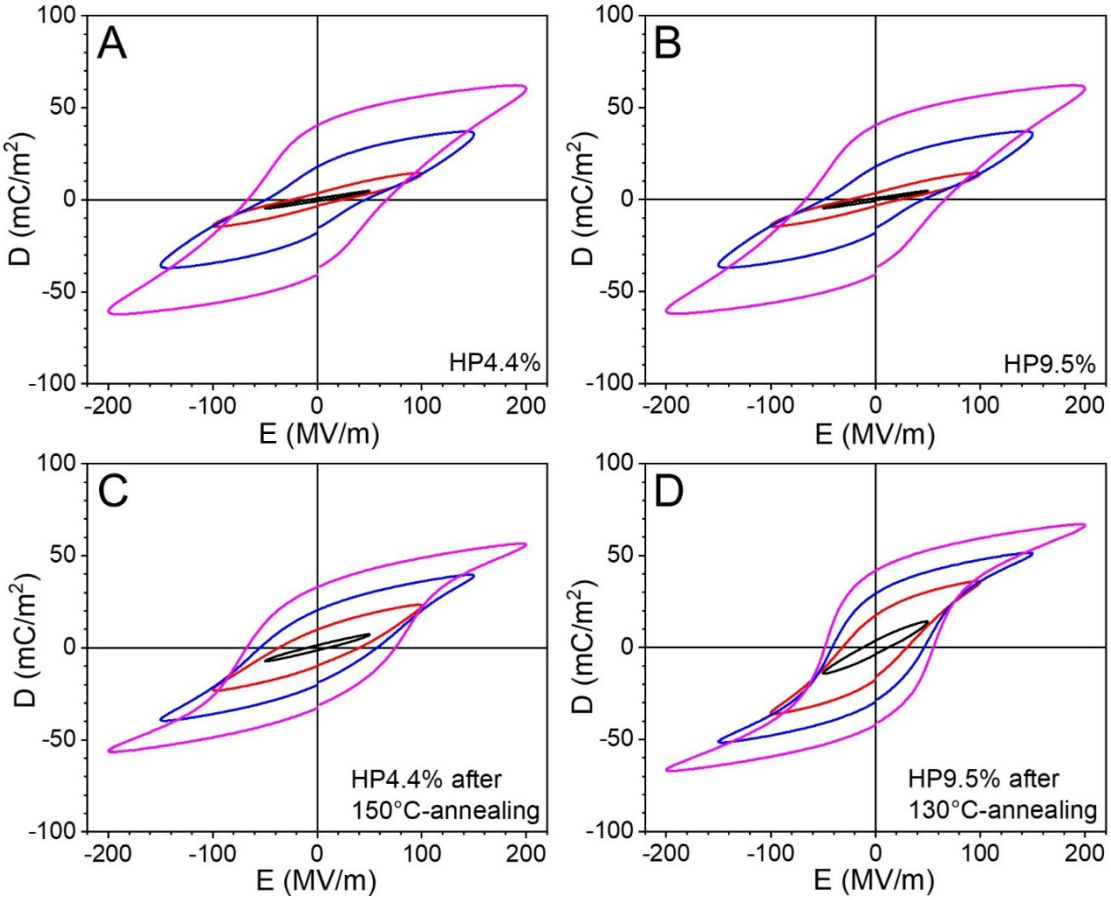

Figure 5. Bipolar D-E loops for (A,B) HP4.4% and (C,D) HP9.5% (A,C) before and (B,D) after thermal annealing above the T_C (i.e., 150 °C for HP4.4% and 130 °C for HP9.5%). The tests were performed at room temperature, and the poling frequency was 10 Hz with a sinusoidal waveform.

The ferroelectric behavior for the high-pressure crystallized samples was studied using bipolar D-E loop tests, and results are shown in Figures 5A and B. Below 100 MV/m, both samples exhibited a linear dielectric behavior. Possibly, bulky CTFE kinks prevented FE switching for the γ crystals. Above 100 MV/m, they displayed obvious FE switching from large domains. After thermal annealing above the T_C for 5 min, both samples became more FE. This was reflected by the broad loops when the poling field was only 100 MV/m. With further increasing the poling field, more significant FE switching was observed. We speculate that certain CTFE kinks should be kicked out of the crystalline region and the FE γ domain grew larger. As a result, the ferroelectricity was enhanced for these samples annealed above the T_C. From these result, it is clear that inclusion of CTFE kinks inside extended chain crystalline lamellae did not lead to the RFE behavior. Instead, large γ domains dictated the normal FE behavior for the high-pressure crystallized samples.

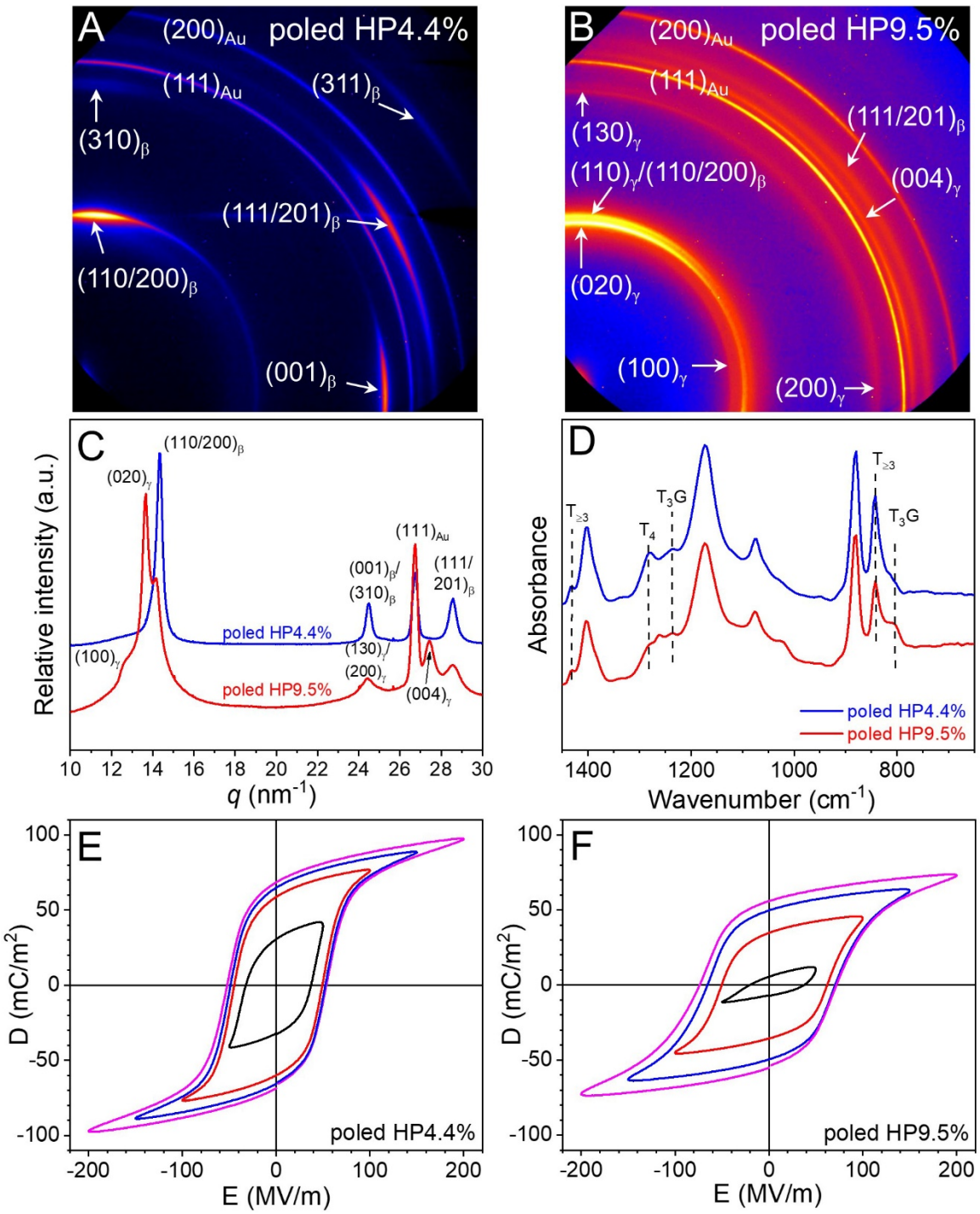

Figure 6. 2D WAXD patterns for (A) HP4.4% and (B) HP9.5% after unipolar poling at 200 MV/m and room temperature for 20 cycles (10 Hz). The corresponding 1D WAXD profiles are shown in (C). The X-ray beam was directed along the transverse direction of the films. (D) FTIR spectra of the above poled HP4.4% and HP9.5% samples. The FTIR was recorded in the ATR mode since the high-pressure crystallized samples were too thick for transmission IR. Bipolar D-E loops for (E) poled HP4.4% and (F) poled HP9.5% at room temperature (10 Hz with a sinusoidal waveform).

From Figure 5, it was observed that high-field electric poling (i.e., >150 MV/m) could induce the formation of large FE domains for high-pressure crystallized samples. It would be interesting to see how electric poling changed the crystalline structure and the subsequent FE behavior. Figures 6A and B show 2D WAXD patterns for the HP4.4% and HP9.5% after unipolar poling at 200 MV/m and room temperature for 20 cycles (10 Hz). The corresponding 2D SAXS patterns are shown in Figure S6. The integrated 1D WAXD profiles are shown in Figure 6C. From Figures 6A and C, the poled HP4.4% sample exhibited a uniaxially oriented β crystalline structure with *c*-axis in the horizontal direction, and no reflections from the γ phase could be seen. Therefore, 20 cycles of unipolar poling at 200 MV/m resulted in a pure β phase for HP4.4%. This was also reflected in the FTIR spectrum for the poled HP4.4% in Figure 6D with an obvious T_4 absorption band at 1276 cm^{-1}. Because of the pure β phase in poled HP4.4%, the FE switching became significant with a maximum D (D_{max}) of 97 mC/m^2 at 200 MV/m. This value was significantly higher than that (60 mC/m^2) for the nascent HP4.4% sample with a pure γ phase (Figure 5A).

The situation for HP9.5% was different. As shown in Figures 6B and D, the γ phase largely persisted after 20 cycles of unipolar poling at room temperature. Only a shoulder $(110/200)_\beta$ at 14.1 nm^{-1} and a $(111/201)_\beta$ reflection at 28.5 nm^{-1} were seen, indicating certain γ phase had transformed into the β phase upon electric poling. FTIR spectrum in Figure 6D confirmed the major γ phase. Because of this major γ phase, the D-E loops for the poled HP9.5% sample exhibited a lower D_{max} (70 MV/m) at 200 MV/m than that (97 MV/m) for the poled HP4.4% with a pure β phase. Meanwhile, the coercive field (E_C) at the 200 MV/m poling field was also higher for the poled HP9.5% (72 MV/m) than that (54 MV/m) for the poled HP4.4%. We consider that the amount of CTFE defects was too high to be kicked out from the extended-chain crystals for the HP9.5% sample. This prevented the phase transition into the β phase when the poling field

was 200 MV/m. At the same time, the CTFE kinks in poled HP9.5% prevented easy FE switching and thus resulted in a higher E_C.

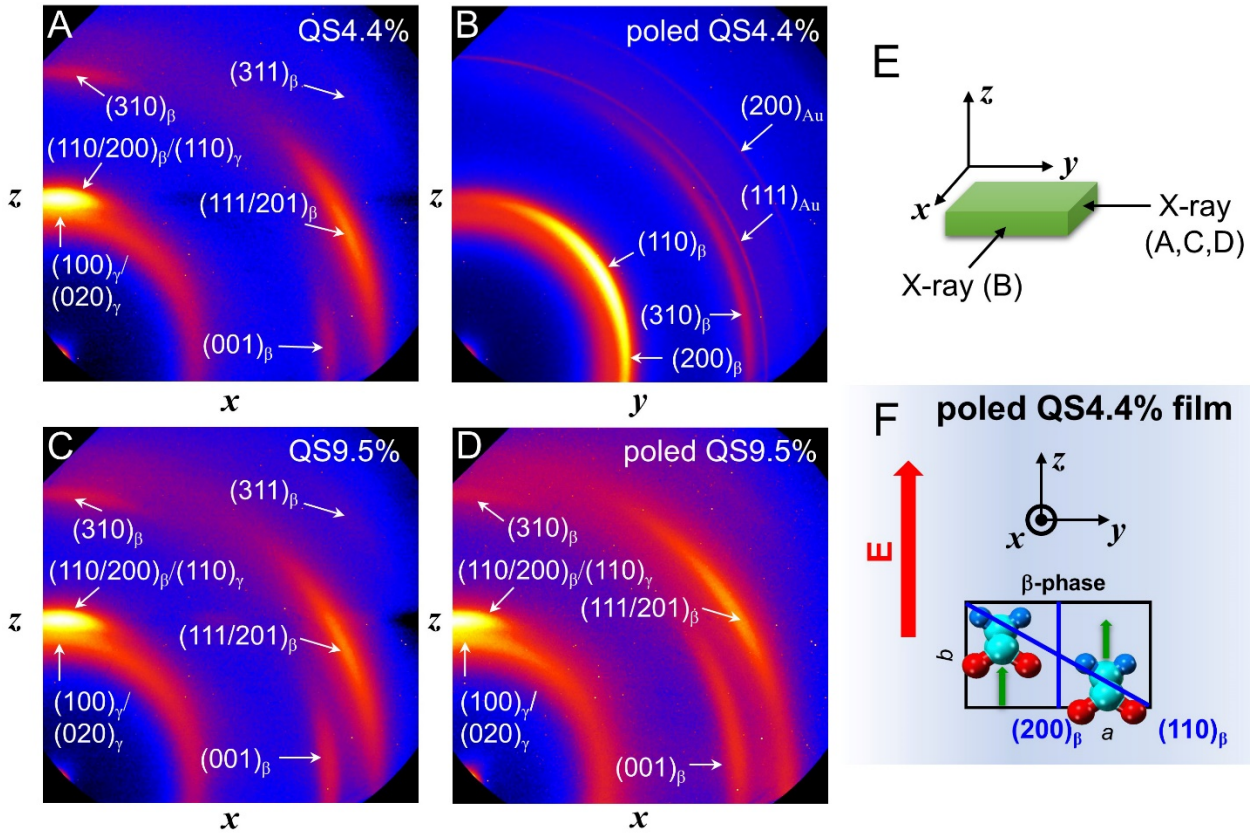

Figure 7. 2D WAXD patterns for (A,B) QS4.4% and (C,D) QS9.5% (A,C) before and (B,D) after unipolar poling at 200 MV/m and room temperature for 20 cycles (10 Hz). (E) The stretching direction for the QS samples is along *x*, the film thickness direction is *z*, and the transverse direction is *y*. The X-ray beam was directed along the *y* direction for (A,C,D) and along the *x* direction for (B). (F) Schematic representation of the β unit cell orientation in the poled QS4.4% film in (B).

Low-Temperature Uniaxial Stretching for Quenched and Stretched P(VDF-CTFE) Films and Their Ferroelectric Properties. As reported recently, mechanical stretching could pull large comonomers (e.g., CTFE[29] or even HFP[30]), which otherwise are excluded from the crystals, into the crystalline region [i.e., the P(VDF-TrFE) crystals] to form isomorphic crystals and thus nanodomains for the RFE behavior. In addition, mechanical stretching could break up

large crystals into small crystallites via plastic deformation.[42] It has also been reported that low-temperature stretching of PVDF would result in more oriented β crystals.[43-45] Here, we propose to uniaxially stretch quenched P(VDF-CTFE) films between -20 ~ 0 °C to see if CTFE could be pulled into PVDF crystals and how small crystallite size will affect the ferroelectric property. Figures 7A-D show 2D WAXD patterns for the QS4.4% and QS9.5% films before and after electric poling (200 MV/m at room temperature for 20 cycles), respectively. The X-ray beam was directed along the transverse *y* direction, except for the poled QS4.4% in Figure 7B, where the X-ray beam was along the stretching direction *x*. Corresponding 2D SAXS patterns for QS4.4% and QS9.5% are shown in Figures S7 and S8, respectively. The integrated 1D WAXD profiles are shown in Figures 8A and B. From the 1D WAXD profiles in Figure 8A, the QS4.4% exhibited major β phase with broad $(110/200)_\beta$, $(001)_\beta$, $(310)_\beta$, and $(111/201)_\beta$ reflections, consistent with prior reports that low-temperature stretching favored the polar β phase.[44, 45] Using the Scherrer estimation, the average crystallite size was estimated to be 6.5 nm for the $(111/201)_\beta$ reflection (see Figures S9A/B). Indeed, the crystallite size was fairly small after uniaxial stretching. From the 2D pattern (Figure 7A) and 1D WAXD profiles for the QS4.4% (Figure 8A), it was not certain whether it contained any γ phase or not. However, after electric poling (Figure 7B), the 1D WAXD profile showed only reflections from the β phase, i.e., $(110/200)_\beta$ and $(310)_\beta$, suggesting that electric poling at 200 MV/m for 20 cycles also resulted in a pure β phase for the poled QS4.4%. However, comparing the 1D WAXD profiles before and after electric poling for QS4.4% (Figure 8A), it was clear that the broad and mixed $(100)_\gamma/(020)_\gamma$ reflections were present for QS4.4%. From the reflection intensity, the γ phase should be a minor component. Note that the 2D WAXD patterns along the *y* direction usually showed a uniaxial pattern along the *c*-axis of PVDF crystals, because the stretching direction was along *x*. However, after electric poling for QS4.4%, the dipole

direction or the *b*-axis was aligned along the field direction normal to the film (see the scheme in Figure 7F). As a result, the $(110)_\beta/(200)_\beta$ would be out of the diffraction condition when the X-ray beam was directed along *y* (see the rightmost WAXD pattern in Figure S7; only a broad halo was observed in the 1D WAXD profile for the X-ray beam along *y*). To prove this explanation, we performed a WAXD experiment for X-ray along *x*, and the 2D pattern is shown in Figure 7B. Indeed, the $(110)_\beta$ was observed tilted in the quadrant and the $(200)_\beta$ was in the horizontal direction. The poling induced γ-to-β phase transition in QS4.4% was less obvious in FTIR spectra (Figure 8C), because β and γ phases shared many overlapped absorption bands. The only difference was the 1234 cm^{-1} band for the γ phase, whose intensity decreased slightly after electric poling.

For QS9.5%, uniaxial stretching also induced the formation of mixed β and γ crystals with typical crystalline reflections (Figure 7C). Judging from the peak intensities in Figure 8B, the β phase should be the majority and the γ phase should be the minority. However, since β and γ phases had overlapped X-ray and FTIR peaks, it was difficult to quantitatively determine their relative contents. After unipolar poling, the 2D WAXD pattern along *y* still displayed a significant uniaxial crystal orientation with mixed β and γ reflections (Figure 7D). From the 1D profile in Figure 8B, the $(110/200)_\beta$ intensity decreased somewhat. This again could be explained by the alignment of β dipoles (i.e., the *b*-axis) along the poling field direction normal to the film. Consequently, these $(110/200)_\beta$ reflections would be out of the diffraction condition for the *y* WAXD pattern. Therefore, the $(110/200)_\beta$ peak decreased intensity after poling. Compared to the poled QS4.4%, it was obvious that QS9.5% was more difficult to transform from the γ to the β phase and to align the β dipoles along the field direction by electric poling. This could be explained by the higher content of CTFE defects in QS9.5% than in QS4.4%, which prevented easy dipole rotation by the poling electric field. It was unlikely that the CTFE defects presented as kinks in

the crystalline phase. Otherwise, the QS samples should also exhibit a Curie transition, but no T_C was not observed in the DSC curves (see Figures 2A and B). Therefore, CTFE defects should primarily locate at the crystal-amorphous interfaces. Because the crystallites were small (5.6 nm, estimated from Scherrer equation; see Figures S9C/D), we speculate that these interfacial CTFE defects could influence the dipole switching inside the crystalline phase. Similar phenomenon was also observed for polyethylene copolymers, where the unit cell dimensions were affected by the large comonomers at the crystal-amorphous interfaces.[46] Finally, the FTIR spectra in Figure 8D showed typical absorption bands for $T_{\geq 3}$ and T_3 conformations. Nonetheless, no obvious evidence was seen for the γ-to-β transition by electric poling.

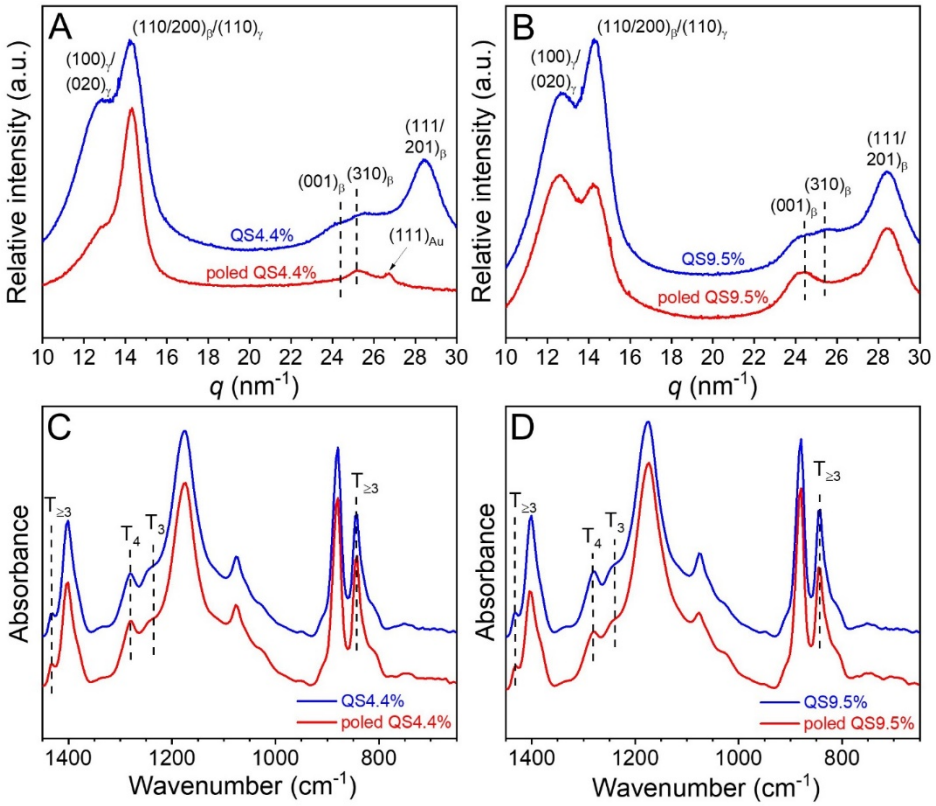

Figure 8. 1D WAXD profiles for (A) QS4.4% and (B) QS9.5% before and after unipolar poling at 200 MV/m and room temperature for 20 cycles (10 Hz). FTIR spectra for (C) QS4.4% and (D) QS9.5% before and after unipolar poling at 200 MV/m and room temperature for 20 cycles (10 Hz). FTIR spectra were obtained in the transmission mode.

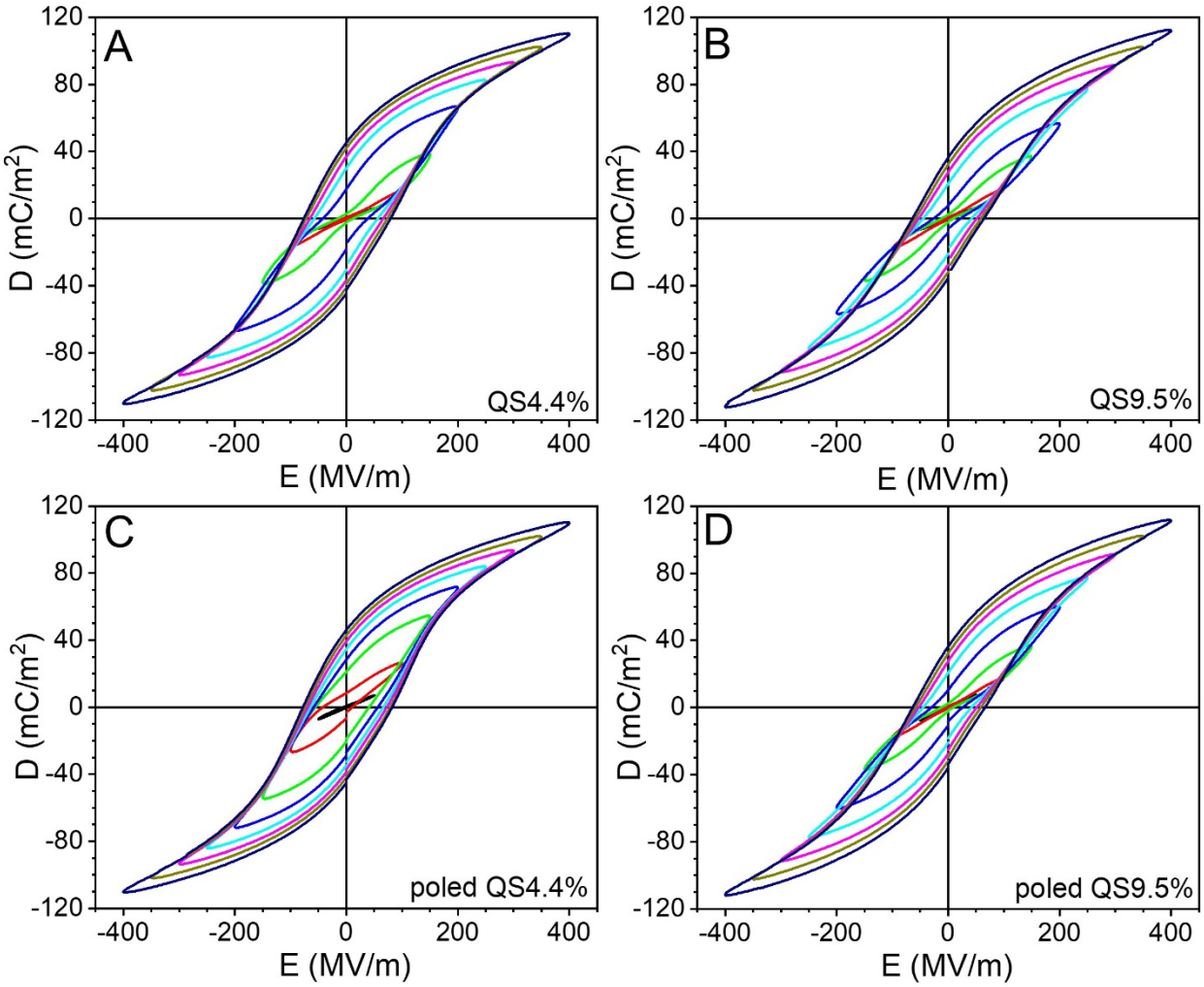

Figure 9. Bipolar D-E loops for (A) QS4.4%, (B) QS9.5%, (C) poled QS4.4%, and (D) poled QS9.5% at room temperature. The poling frequency was 10 Hz with a sinusoidal waveform.

Uniaxial stretching at low temperatures substantially changed the ferroelectric behavior of P(VDF-CTFE) copolymers, as shown in Figure 9. Basically, both QS4.4% and QS9.5% samples showed slimmer FE loops and higher breakdown strengths compared to the Q and HP samples. This could be attributed to the small crystallite sizes (i.e., 6.5 nm for QS4.4% and 5.6 nm for QS9.5%) and thus small FE domain sizes in the samples. From Figures 9A and B, the QS9.5% overall presented slimmer ferroelectric loops than the QS4.4% probably because of the smaller crystallite size for QS9.5% due to more CTFE detects (note that FE domains size is always smaller

than the crystallite size). After unipolar poling, the poled QS4.4% became more FE. For example, the poled QS4.4% exhibited a broad FE loop whereas the QS4.4% only showed a slim DHL when the poling field was 150 MV/m (compare Figure 9C with Figure 9A, and also see Figure S10 for better comparison). However, this was not the case for the poled QS9.5% sample. Namely, no obvious changes were observed after unipolar poling for QS9.5% (compare Figure 9D with Figure 9B). Again, it was likely that the CTFE defects at the crystal-amorphous interfaces prevented easy dipole switching for QS9.5%, consistent with the WAXD results in Figures 7 and 8. From the above D-E loop results, no real RFE behavior was achieved for both QS4.4% and QS9.5% samples.

On the basis of our previous reports,[3, 5] we understand that nanodomains in the size of 2-3 nm are responsible for the RFE behavior, and they could only be achieved by inclusion of large comonomer defects inside the isomorphic crystalline structure. From the above studies, it is clear that localization of CTFE defects at the crystal-amorphous interfaces could not achieve nanodomains as small as 2-3 nm. As a result, no RFE behavior is achieved for either HP or QS samples. Instead, a certain amount of TrFE has to be copolymerized with VDF to include defects from the larger termonomers such as CTFE[29] and HFP.[30] In other words, PVDF crystals are too tightly packed and no larger defects could be accommodated in the crystalline structures, whether the α, γ, or β phase. On the contrary, P(VDF-TrFE) crystals are loosely packed, and larger defects, even HFP, could be included in the crystalline structure with the assistance of mechanical stretching.

Conclusions

To answer the question whether inclusion of CTFE units in PVDF crystals could achieve the RFE behavior for the P(VDF-CTFE) copolymers or not, two samples were synthesized with

4.4 mol.% and 9.5 mol.% CTFE. Two strategies were attempted. The first strategy utilized high-pressure crystallization to include CTFE in PVDF crystals via the pseudohexagonal PE phase. Indeed, extended-chain crystals with lamellar thicknesses of 60-70 nm were obtained for HP4.4% and HP9.5%. However, from WAXD and FTIR structural analyses, both samples exhibited the γ phase of neat PVDF with CTFE units largely excluded from the γ unit cells. It was considered that CTFE units should be included as kinks, which induced a γ-to-PE Curie transition for the extended-chain crystals. Because these kinks did not break up large γ FE domains, the normal FE behavior was observed showing broad hysteresis loops.

The second strategy took advantage of low-temperature stretching to break up large crystals. Structural analysis indicated that small oriented β crystallites (5-7 nm) were obtained for the QS4.4% and QS9.5% samples with a minor γ phase. Again, the CTFE units should be largely excluded from the β/γ unit cells, locating primarily at the crystal-amorphous interfaces. Although the FE loops for the low-temperature stretched samples appeared to be narrower than those of the normal FE behavior, no slim hysteresis loops were observed. This result suggested that external CTFE defects had a less significant impact than the internal CTFE defects to achieve 2-3 nm nanodomains and thus the RFE behavior.

Finally, the effect of electric poling was also studied for various P(VDF-CTFE) samples. Upon unipolar poling at 200 MV/m for 20 cycles, the HP4.4% and QS4.4% samples were easy to transform into the pure β phase. On the contrary, the HP9.5% and QS9.5% samples had limited phase transformation and crystal orientation upon electric poling, owing to a higher content of CTFE defects either in the kinks (for HP9.5%) or at the crystal-amorphous interfaces (for QS9.5%).

From this study, we understand that the CTFE unit is too large to be included into tightly packed PVDF crystals, whether the α, γ, or β phase. It can be included in the crystalline region to

form an isomorphic crystal only when terpolymerized with VDF and TrFE. When the TrFE content is high enough (e.g., >20 mol.%), CTFE can be directly included in the crystalline region upon quiescent crystallization.[3] When the TrFE content is low (<20 mol.%), mechanical stretching can be used to pull CTFE into the isomorphic P(VDF-TrFE) crystals.[29] As a result of isomorphic crystals with CTFE breaking up large domains into 2-3 nm nanodomains, the RFE behavior is achieved for these terpolymers. To achieve the RFE behavior without TrFE, we propose to explore other PVDF copolymers with a smaller termonomer than CTFE, e.g., 1,1-chlorofluoroethylene (CFE). Currently, research is underway to study whether this is possible for P(VDF-CFE) random copolymers.

Author Information

Corresponding Authors

*E-mail: lxz121@case.edu (L.Z.).

*E-mail: liyue1990liyue@gmail.com (Y. Li).

ORICD

Yanfei Huang: 0000-0001-9383-5063

Jia-Zhuang Xu: 0000-0001-9888-7014

Thibaut Soulestin: 0000-0002-1534-0230

Jun Lei: 0000-0001-6803-5216

Gan-Ji Zhong: 0000-0002-8540-7293

Zhong-Ming Li: 0000-0001-7203-1453

Lei Zhu: 0000-0001-6570-9123

Notes

The authors declare no competing financial interest.

Acknowledgements

This work is partially supported by National Science Foundation (DMR-1708990). Y.H. acknowledges financial support from China Scholarship Council (201606240042). Y.L. acknowledges partial financial support from the Fundamental Research Funds for the Central Universities (Grant 2018SCU12005) and China Postdoctoral Science Foundation Funded Project (No. 2018M633364). J.-Z.X. acknowledges partial financial support from the National Natural Science Foundation of China (Grant 51573116). This research used the 11-BM CMS beamline of National Synchrotron Light Source-II (NSLS-II), Brookhaven National Laboratory (BNL), a U.S. Department of Energy User Facility operated for the Office of Science by BNL under contract No. DE-SC0012704. Finally, the authors thank Ms. Qiong Li at Case Western Reserve University for SEC measurements.

Supporting Information. The Supporting Information is available free of charge on the ACS Publications website at DOI: xxxxxxxxxxxxx.

^{19}F and ^{1}H NMR spectra and SEC results for P(VDF-CTFE)-4.4% and P(VDF-CTFE)-9.5%; SAXS results for various P(VDF-CTFE)-4.4% and P(VDF-CTFE)-9.5% films, DSC curves for HP4.4% and HP9.5% crystallized under different combinations of pressure and temperature;

crystallite size estimation using Scherrer equation for QS4.4% and QS9.5% films; Comparison of bipolar D-E loops for QS4.4% and poled QS4.4% at different poling fields.

References

1. Yang, L.; Li, X.; Allahyarov, E.; Taylor, P. L.; Zhang, Q. M.; Zhu, L. Novel polymer ferroelectric behavior via crystal isomorphism and the nanoconfinement effect. *Polymer* **2013,** *54*, 1709-1728.
2. Soulestin, T.; Ladmiral, V.; Dominguez Dos Santos, F.; Ameduri, B. Vinylidene fluoride- and trifluoroethylene-containing fluorinated electroactive copolymers. How does chemistry impact properties? *Prog. Polym. Sci.* **2017,** *72*, 16-60.
3. Zhu, L. Exploring strategies for high dielectric constant and low loss polymer dielectrics. *J. Phys. Chem. Lett.* **2014,** *5*, 3677-3687.
4. Chen, Q.; Shen, Y.; Zhang, S.; Zhang, Q. M. Polymer-based dielectrics with high energy storage density. *Annu. Rev. Mater. Res.* **2015,** *45*, 433-458.
5. Baer, E.; Zhu, L. 50th Anniversary Perspective: Dielectric phenomena in polymers and multilayered dielectric films. *Macromolecules* **2017,** *50*, 2239-2256.
6. Zhang, Q. M.; Huang, C.; Xia, F.; Su, J., Electric EAP. In *Electroactive Polymer (EAP) Actuators as Artificial Muscles: Reality, Potential, and Challenges*, 2nd ed.; Bar-Cohen, Y., Ed.; SPIE Press: 2004; Chapter 4, pp 89-139.
7. Zhang, Q. M.; Bharti, V.; Zhao, X. Giant electrostriction and relaxor ferroelectric behavior in electron-irradiated poly(vinylidene fluoride-trifluoroethylene) copolymer. *Science* **1998,** *280*, 2101-2104.

8. Bharti, V.; Zhao, X. Z.; Zhang, Q. M.; Romotowski, T.; Tito, F.; Ting, R. Ultrahigh field induced strain and polarization response in electron irradiated poly(vinylidene fluoride-trifluoroethylene) copolymer. *Mater. Res. Innovations* **1998,** *2*, 57-63.

9. Chen, X.; Han, X.; Shen, Q.-D. PVDF-based ferroelectric polymers in modern flexible electronics. *Adv. Electron. Mater.* **2017,** *3*, 1600460.

10. Han, X.; Chen, X.; Tang, X.; Chen, Y.-L.; Liu, J.-H.; Shen, Q.-D. Flexible polymer transducers for dynamic recognizing physiological signals. *Adv. Funct. Mater.* **2016,** *26*, 3640-3648.

11. Chu, B.; Zhou, X.; Ren, K.; Neese, B.; Lin, M. R.; Wang, Q.; Bauer, F.; Zhang, Q. M. A dielectric polymer with high electric energy density and fast discharge speed. *Science* **2006,** *313*, 334-336.

12. Zhu, L.; Wang, Q. Novel ferroelectric polymers for high energy density and low loss dielectrics. *Macromolecules* **2012,** *45*, 2937-2954.

13. Neese, B.; Chu, B.; Lu, S.-G.; Wang, Y.; Furman, E.; Zhang, Q. M. Large electrocaloric effect in ferroelectric polymers near room temperature. *Science* **2008,** *321*, 821-823.

14. Moya, X.; Kar-Narayan, S.; Mathur, N. D. Caloric materials near ferroic phase transitions. *Nat. Mater.* **2014,** *13*, 439-450.

15. Lovinger, A. J. Polymorphic transformations in ferroelectric copolymers of vinylidene fluoride induced by electron-irradiation. *Macromolecules* **1985,** *18*, 910-918.

16. Chung, T. C.; Petchsuk, A. Synthesis and properties of ferroelectric fluoroterpolymers with Curie transition at ambient temperature. *Macromolecules* **2002,** *35*, 7678-7684.

17. Xia, F.; Cheng, Z.; Xu, H.; Li, H.; Zhang, Q.; Kavarnos, G. J.; Ting, R. Y.; Abdul-Sadek, G.; Belfield, K. D. High electromechanical responses in a poly(vinylidene fluoride-trifluoroethylene-chlorofluoroethylene) terpolymer. *Adv. Mater.* **2002,** *14*, 1574-1577.

18. Samara, G. A. The relaxational properties of compositionally disordered ABO_3 perovskites. *J. Phys.: Condens. Matter* **2003,** *15*, R367-R411.

19. Ye, Z. G. Relaxor ferroelectric complex perovskites: Structure, properties and phase transitions. *Key Eng. Mater.* **1998,** *155-156*, 81-122.

20. Bokov, A. A.; Ye, Z. G. Recent progress in relaxor ferroelectrics with perovskite structure. *J. Mater. Sci.* **2006,** *41*, 31-52.

21. Boulesteix, C.; Varnier, F.; Llebaria, A.; Husson, E. Numerical determination of the local ordering of $PbMg_{1/3}Nb_{2/3}O_3$ (PMN) from high resolution electron microscopy images. *J. Solid State Chem.* **1994,** *108*, 141-147.

22. Yoshida, M.; Mori, S.; Yamamoto, N.; Uesu, Y.; Kiat, J. M. TEM observation of polar domains in relaxor ferroelectric $Pb(Mg_{1/3}Nb_{2/3})O_3$. *Ferroelectrics* **1998,** *217*, 327-333.

23. Mabboux, P. Y.; Gleason, K. K. ^{19}F NMR characterization of electron beam irradiated vinylidene fluoride-trifluoroethylene copolymers. *J. Fluorine Chem.* **2002,** *113*, 27-35.

24. Wang, L.; Zhao, X.; Feng, J. Effects of electron irradiation on poly(vinylidene fluoride-trifluoroethylene) copolymers studied by solid-state nuclear magnetic resonance spectroscopy. *J. Polym. Sci., Part B: Polym. Phys.* **2006,** *44*, 1714-1724.

25. Zhang, Z.; Litt, M. H.; Zhu, L. Achieving relaxor ferroelectric-like behavior in nylon random copolymers and terpolymers. *Macromolecules* **2017,** *50*, 9360-9372.

26. Yang, L.; Tyburski, B. A.; Domingues Dos Santos, F.; Endoh, M. K.; Koga, T.; Huang, D.; Wang, Y.; Zhu, L. Relaxor ferroelectric behavior from strong physical pinning in a

poly(vinylidene fluoride-*co*-trifluoroethylene-*co*-chlorotrifluoroethylene) random terpolymer. *Macromolecules* **2014,** *47*, 8119-8125.

27. Furukawa, T. Structure and functional properties of ferroelectric polymers. *Adv. Colloid Interface Sci.* **1997,** *71-72*, 183-208.
28. Hattori, T.; Watanabe, T.; Akama, S.; Hikosaka, M.; Ohigashi, H. The high-pressure crystallization behaviours and piezoelectricity of extended chain lamellar crystals of vinylidene fluoride trifluoroethylene copolymers with high molar content of vinylidene fluoride. *Polymer* **1997,** *38*, 3505-3511.
29. Gadinski, M. R.; Li, Q.; Zhang, G.; Zhang, X.; Wang, Q. Understanding of relaxor ferroelectric behavior of poly(vinylidene fluoride-trifluoroethylene-chlorotrifluoroethylene) terpolymers. *Macromolecules* **2015,** *48*, 2731-2739.
30. Li, Y.; Soulestin, T.; Ladmiral, V.; Ameduri, B.; Lannuzel, T.; Dominguez Dos Santos, F.; Li, Z.-M.; Zhong, G.-J.; Zhu, L. Stretching-induced relaxor ferroelectric behavior in a poly(vinylidene fluoride-*co*-trifluoroethylene-*co*-hexafluoropropylene) random terpolymer. *Macromolecules* **2017,** *50*, 7646-7656.
31. Zhou, X.; Chu, B.; Neese, B.; Lin, M.; Zhang, Q. M. Electrical energy density and discharge characteristics of a poly(vinylidene fluoride-chlorotrifluoroethylene) copolymer. *IEEE Trans. Dielectr. Electr. Insul.* **2007,** *14*, 1133-1138.
32. Zhou, X.; Zhao, X.; Suo, Z.; Zou, C.; Runt, J.; Liu, S.; Zhang, S.; Zhang, Q. M. Electrical breakdown and ultrahigh electrical energy density in poly(vinylidene fluoride-hexafluoropropylene) copolymer. *Appl. Phys. Lett.* **2009,** *94*, 162901.

33. Guan, F.; Yang, L.; Wang, J.; Guan, B.; Han, K.; Wang, Q.; Zhu, L. Confined ferroelectric properties in poly(vinylidene fluoride-*co*-chlorotrifluoroethylene)-*graft*-polystyrene graft copolymers for electric energy storage applications. *Adv. Funct. Mater.* **2011,** *21*, 3176-3188.

34. Vaughan, A. S. Etching and morphology of poly(vinylidene fluoride). *J. Mater. Sci.* **1993,** *28*, 1805-1813.

35. Nakagawa, K.; Ishida, Y. Annealing effects in poly(vinylidene fluoride) as revealed by specific volume measurements, differential scanning calorimetry, and electron microscopy. *J. Polym. Sci., Part B: Polym. Phys.* **1973,** *11*, 2153-2171.

36. Gradys, A.; Sajkiewicz, P.; Adamovsky, S.; Minakov, A.; Schick, C. Crystallization of poly(vinylidene fluoride) during ultra-fast cooling. *Thermochim. Acta* **2007,** *461*, 153-157.

37. Pan, M.; Yang, L.; Wang, J.; Tang, S.; Zhong, G.; Su, R.; Sen, M. K.; Endoh, M. K.; Koga, T.; Zhu, L. Composite poly(vinylidene fluoride)/polystyrene latex particles for confined crystallization in 180 nm nanospheres via emulsifier-free batch seeded emulsion polymerization. *Macromolecules* **2014,** *47*, 2632-2644.

38. Yang, L.; Ho, J.; Allahyarov, E.; Mu, R.; Zhu, L. Semicrystalline structure-dielectric property relationship and electrical conduction in a biaxially oriented poly(vinylidene fluoride) film under high electric fields and high temperatures. *ACS Appl. Mater. Interfaces* **2015,** *7*, 19894-19905.

39. Tashiro, K., Crystal structure and phase transition of PVDF and related copolymers. In *Ferroelectric Polymers: Chemistry, Physics, and Applications*; Nalwa, H. S., Ed.; Marcel Dekker: New York, 1995; Chapter 2, pp 63-182.

40. Bachmann, M. A.; Gordon, W. L.; Koenig, J. L.; Lando, J. B. Infrared study of phase-III poly(vinylidene fluoride). *J. Appl. Phys.* **1979,** *50*, 6106-6112.

41. Tashiro, K.; Tanaka, R. Structural correlation between crystal lattice and lamellar morphology in the ferroelectric phase transition of vinylidene fluoride-trifluoroethylene copolymers as revealed by the simultaneous measurements of wide-angle and small-angle X-ray scatterings. *Polymer* **2006,** *47*, 5433-5444.

42. Galeski, A. Strength and toughness of crystalline polymer systems. *Prog. Polym. Sci.* **2003,** *28*, 1643-1699.

43. Salimi, A.; Yousefi, A. A. FTIR studies of β-phase crystal formation in stretched PVDF films. *Polym. Test.* **2003,** *22*, 699-704.

44. Sencadas, V.; Gregorio, R.; Lanceros-Mendez, S. α to β phase transformation and microestructural changes of PVDF films induced by uniaxial stretch. *J. Macromol. Sci. B* **2009,** *48*, 514-525.

45. Guo, H.; Zhang, Y.; Xue, F.; Cai, Z.; Shang, Y.; Li, J.; Chen, Y.; Wu, Z.; Jiang, S. In-situ synchrotron SAXS and WAXS investigations on deformation and alpha-beta transformation of uniaxial stretched poly(vinylidene fluoride). *CrystEngComm* **2013,** *15*, 1597-1606.

46. Howard, P. R.; Crist, B. Unit-cell dimensions in model ethylene butene-1 copolymers. *J. Polym. Sci., Part B: Polym. Phys.* **1989,** *27*, 2269-2282.

TOC Graphic

Can Relaxor Ferroelectric-like Behavior be Achieved for Poly(vinylidene fluoride-co-chlorotrifluoroethylene) [P(VDF-CTFE)] Random Copolymers by Inclusion of CTFE Units in PVDF Crystals?

Yanfei Huang, Jia-Zhuang Xu, Thibaut Soulestin, Fabrice Domingues Dos Santos, Ruipeng Li, Masafumi Fukuto, Jun Lei, Gan-Ji Zhong, Zhong-Ming Li, Yue Li*, and Lei Zhu*

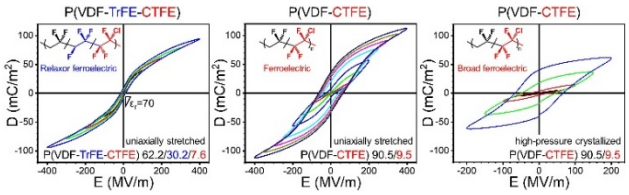

Supporting Information

Can Relaxor Ferroelectric Behavior be Realized for Poly(vinylidene fluoride-*co*-chlorotrifluoroethylene) [P(VDF-CTFE)] Random Copolymers by Inclusion of CTFE Units in PVDF Crystals?

Yanfei Huang,[†,‡,¶] Jia-Zhuang Xu,[†,¶] Thibaut Soulestin,[§] Fabrice Domingues Dos Santos,[§] Ruipeng Li,[#] Masafumi Fukuto,[#] Jun Lei,[†] Gan-Ji Zhong,[†] Zhong-Ming Li,[†] Yue Li,[†,*] and Lei Zhu[‡,*]

[†] *College of Polymer Science and Engineering, State Key Laboratory of Polymer Materials Engineering, Sichuan University, Chengdu 610065, Sichuan, P. R. China*
[‡] *Department of Macromolecular Science and Engineering and Department of Chemistry, Case Western Reserve University, Cleveland, Ohio 44106-7202, United States*
[§] *Piezotech S.A.S., Arkema-CRRA, rue Henri-Moissan, 69493 Cedex Pierre-Benite, France*
[#] *National Synchrotron Light Source II, Brookhaven National Laboratory, Upton, New York 11973, United States*

[¶] These authors contributed equally to the work.

[*] Corresponding authors. Emails: lxz121@case.edu (L. Zhu) and liyue1990liyue@gmail.com (Y. Li).

1. ^{19}F and ^{1}H NMR Spectra for P(VDF-CTFE) Samples

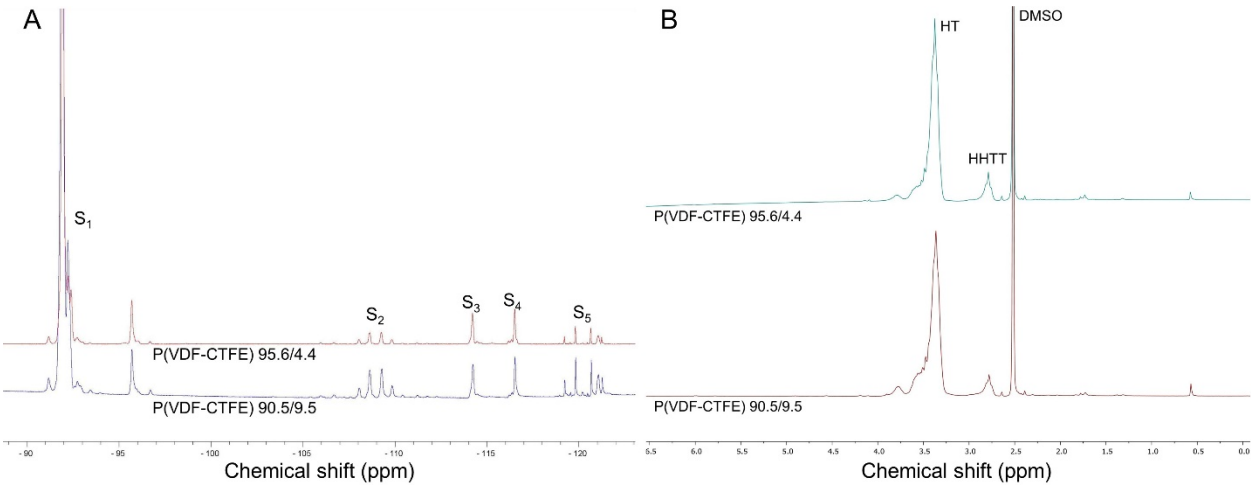

Figure S1. (A) ^{19}F and (B) ^{1}H NMR spectra for P(VDF-CTFE) 95.6/4.4 and 90.5/9.5 (mol./mol.) samples. DMSO-d_6 was used as the solvent. For ^{1}H NMR in (B), a small amount of trifluoroacetic acid (TFA) was added to shift the water peak to low fields (i.e., > 8 ppm).

From ^{19}F NMR spectra, the CTFE content in P(VDF-CTFE) random copolymers can be calculated based on peak assignments in Table S1 and the following equation:[S1]

$$\frac{VDF\%}{CTFE\%} = \frac{3}{2}\frac{S_1+S_2+3S_3-S_4}{S_5+2(S_4-S_3)} \quad (1)$$

From the peak integration results, the CTFE contents were calculated to be 4.4% and 9.5% in mole fraction for the two samples. From the ^{1}H NMR spectra in Figure S1B, the head-to-head and tail-to-tail (HHTT) contents in the long VDF sequence could be calculated to be 9.6 mol.% and 7.8 mol.%, respectively. These HHTT contents were higher than those in PVDF homopolymers (i.e., 3-6%). We speculate that CTFE comonomers might have disrupted the HT sequence and generated more HHTT sequence.

Table 1. ^{19}F NMR Peak Assignments for Different Sequences in P(VDF-CTFE).

Peak area	Sequence	-δ (ppm)
S_1	-$CF_2CH_2CF_2CH_2CF_2$-	91.9
	-$CFClCH_2CF_2CH_2CF_2$-	92.2
	-$CF_2CH_2CF_2CH_2CH_2$-	95.6
S_2	-$CF_2CH_2CF_2CF_2CFCl$-	105.0-113.0
S_3	-$CF_2CH_2CF_2CF_2CH_2$-	113.2
S_4	-$CH_2CF_2CF_2CH_2CH_2$-	116.5
	-$CH_2CF_2CF_2CFClCF_2$-	
S_5	-$CH_2CF_2CF_2CFClCH_2$-	119.0-123.0
	-$CF_2CF_2CFClCH_2CF_2$-	

2. SEC Results for P(VDF-CTFE) Samples

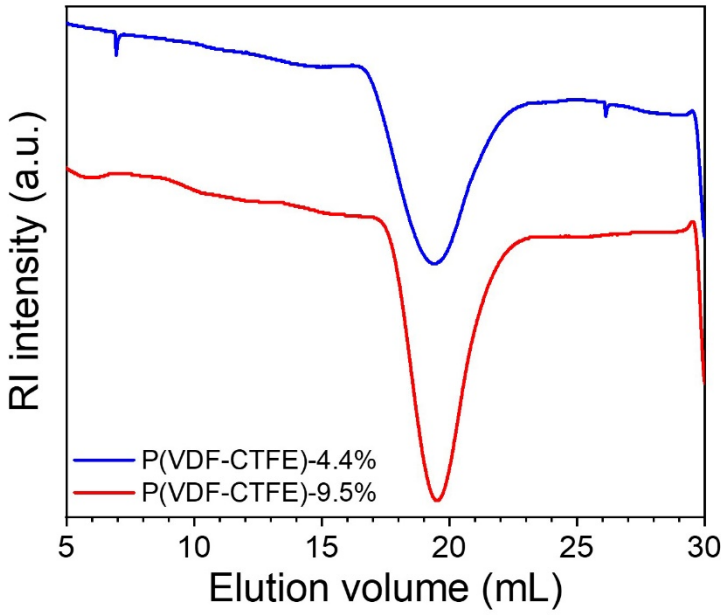

Figure S2. SEC curves for P(VDF-CTFE)-4.4% and P(VDF-CTFE)-9.5%, respectively. DMF was used as the solvent with a flow rate of 1.0 mL/min. Polystyrene standards were used for conventional calibration. Because the refractive index (RI) of P(VDF-CTFE) is lower than that of DMF (1.4305 at 20 °C), negative peaks are obtained.

3. 1D and 2D SAXS Results for Q4.4% and Q9.5%

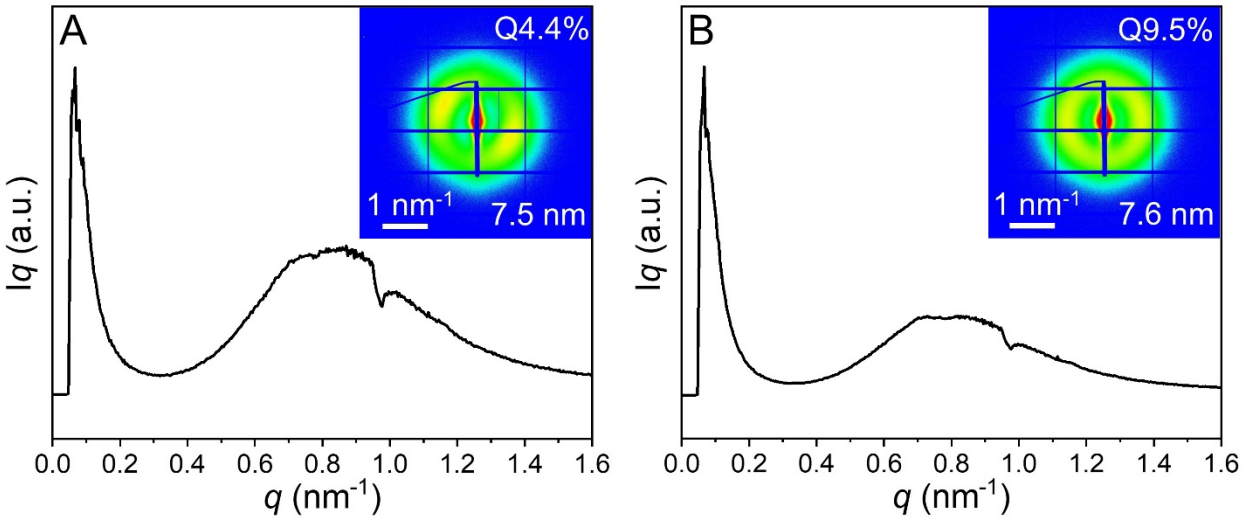

Figure S3. 1D and 2D SAXS results for (A) Q4.4% and (B) Q9.5%, respectively. The lamellar long periods are 7.5 nm for Q4.4% and 7.6 nm Q9.5%. The X-ray beam was directed in the edge-on direction of the film samples.

4. DSC Melting Thermograms for QS P(VDF-CTFE) Samples Crystallized under Various Combinations of Pressure and Temperature

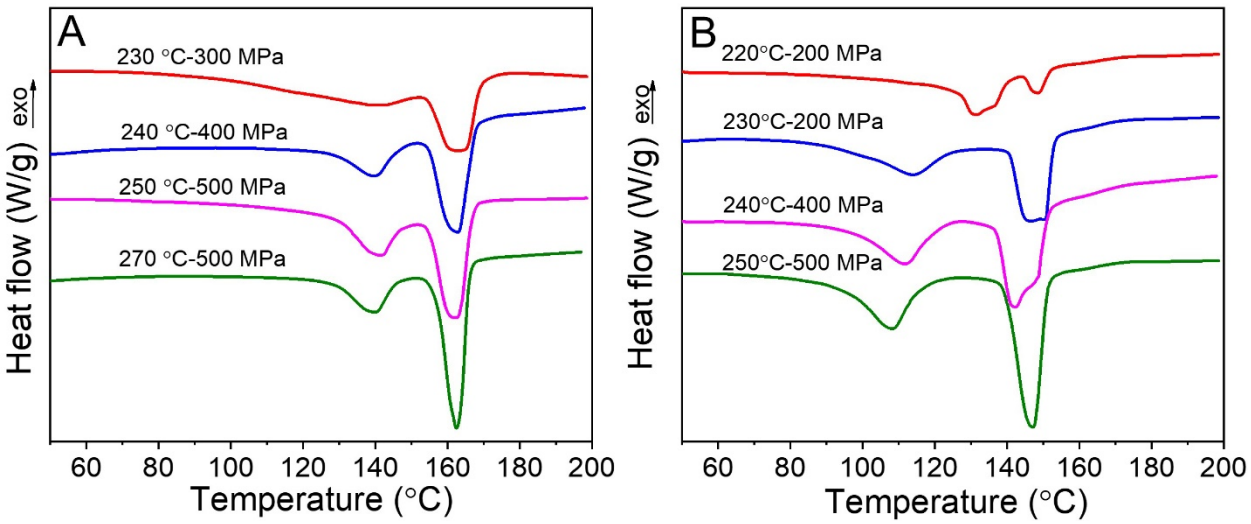

Figure S4. First heating DSC thermograms for (A) HP4.4% and (B) HP9.5% crystallized under various pressure and temperature combinations. The heating rate was 10 °C/min. The best conditions for the formation of extended chain crystals without significant degradation for HP4.4% and HP9.5% are 250 °C under 500 MPa pressure.

5. 2D and 1D SAXS Results for HP4.4% and HP9.5% at Different Temperatures

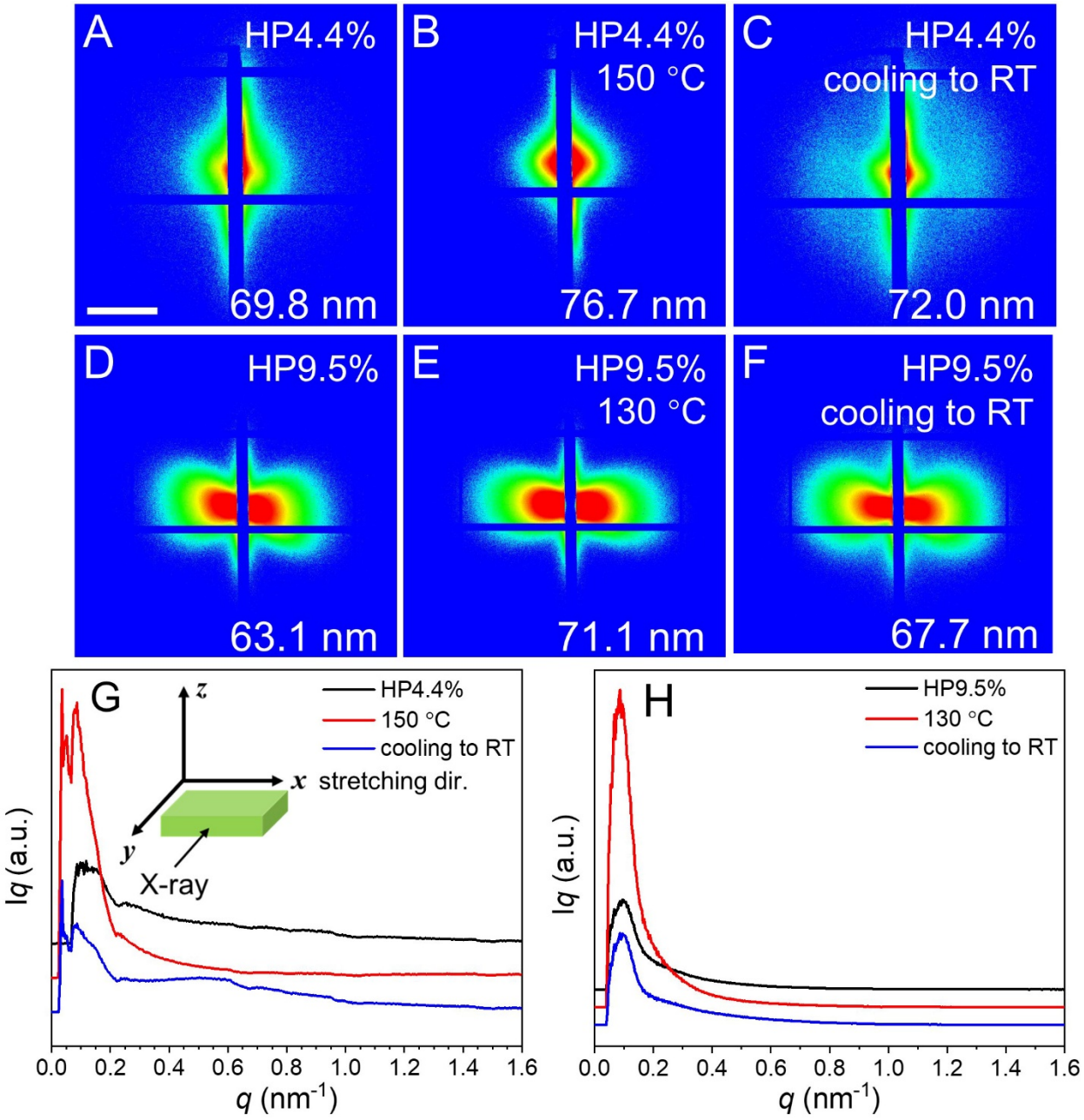

Figure S5. 2D SAXS patterns for (A-C) HP4.4% and (D-F) HP9.5% at (A,D) room temperature, (B) 150 °C for HP4.4% and (E) 130 °C for HP9.5%, and (C,F) cooling back to room temperature. The scale bar is 0.5 nm^{-1}. Corresponding integrated 1D SAXS profiles for (G) HP4.4% and (H) HP9.5% at various temperatures. The X-ray beam was directed in the transverse *y* direction to the film samples.

6. 2D SAXS Patterns for Poled HP4.4% and HP9.5%

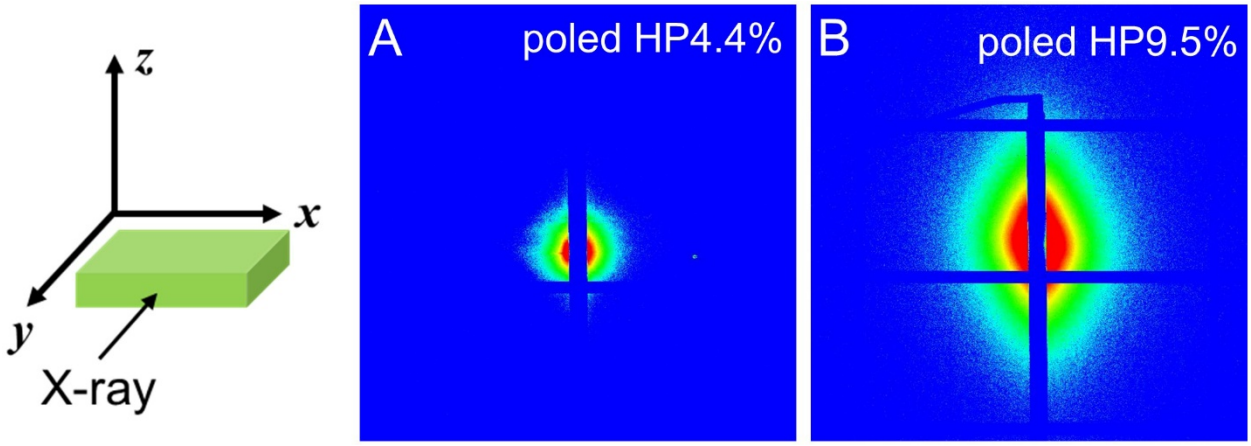

Figure S6. 2D SAXS patterns for poled (A) HP4.4% and (B) HP9.5%, respectively. Both samples were polarized at 200 MV/m (10 Hz) for 20 cycles at room temperature. The X-ray beam was directed in the transverse *y* direction of the film samples.

7. 2D SAXS and WAXD Patterns for QS4.4% and QS9.5% Before and After Unipolar Poling

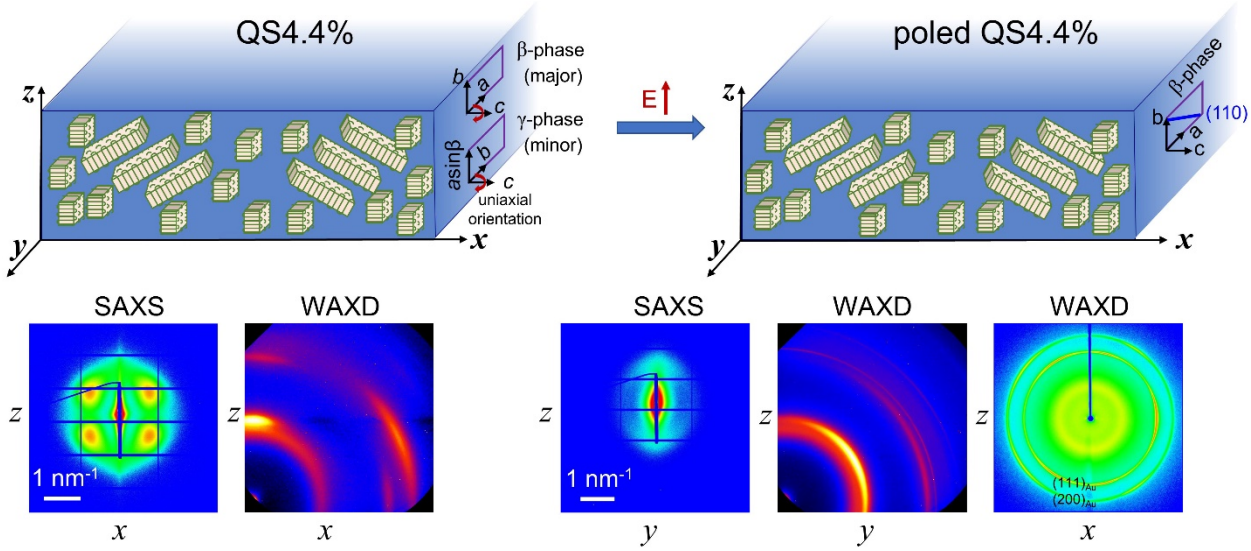

Figure S7. (Top panel) Schematic representation of QS4.4% before and after unipolar poling (200 MV/m at 10 Hz for 20 cycles). (Bottom panel) 2D SAXS and WAXD patterns for the QS4.4% films before and after unipolar poling. The *x*-direction is the stretching direction, the *z* direction is the film normal direction, and the *y* direction is the transverse direction. The X-ray beam was directed along either the *y* or the *x* direction.

For the QS4.4% sample before poling, the WAXD pattern showed a uniaxial crystal orientation along the *c*-axes. However, the SAXS pattern displayed a tilted lamellar pattern, which did not fit to the uniaxial WAXD pattern. To explain both patterns for the unpoled QS4.4%, a schematic representation of crystal organization is proposed in the top left panel of Figure S7. As a result

of CTFE defects in the -$(CH_2CH_2)_n$- sequences, there could be a broad distribution of crystallite sizes. Upon uniaxial stretching, small crystallites (mostly β phase with a minor γ phase) were oriented with their axes aligned parallel to the drawing direction, and most likely they were not regularly stacked. However, relatively large crystallites stacked together and oriented tilted to the drawing direction. Therefore, a butterfly-type of SAXS pattern was obtained for the relatively large lamellar crystals. Because these tilted crystal lamellae were not in the diffraction condition for WAXD along *y*, only the uniaxial WAXD pattern was observed for small crystallites. After unipolar poling at 200 MV/m and 10 Hz for 20 cycles, the small crystallites became the pure β phase with their *b*-axes aligned parallel to the film normal/electric field direction. As a result, no $(110/200)_\beta$ reflection should be seen when the X-ray was directed in the *y* direction. This was exactly seen in the right most WAXD pattern when the X-ray was along *y*. In order to see the $(110)_\beta$ and $(200)_\beta$ reflections, the X-ray beam had to be directed along the *x* direction, and corresponding 2D SAXS and WAXD patterns are shown in the right panel of Figure S7. SAXS showed no lamellar stacking, and the 2D WAXD pattern showed tilted $(110)_\beta$ in the quadrant and $(200)_\beta$ in the horizontal direction. Again, the tilted large crystalline lamellae did not change their orientation and they were not in the diffraction condition to show any reflections when X-ray was along *x*.

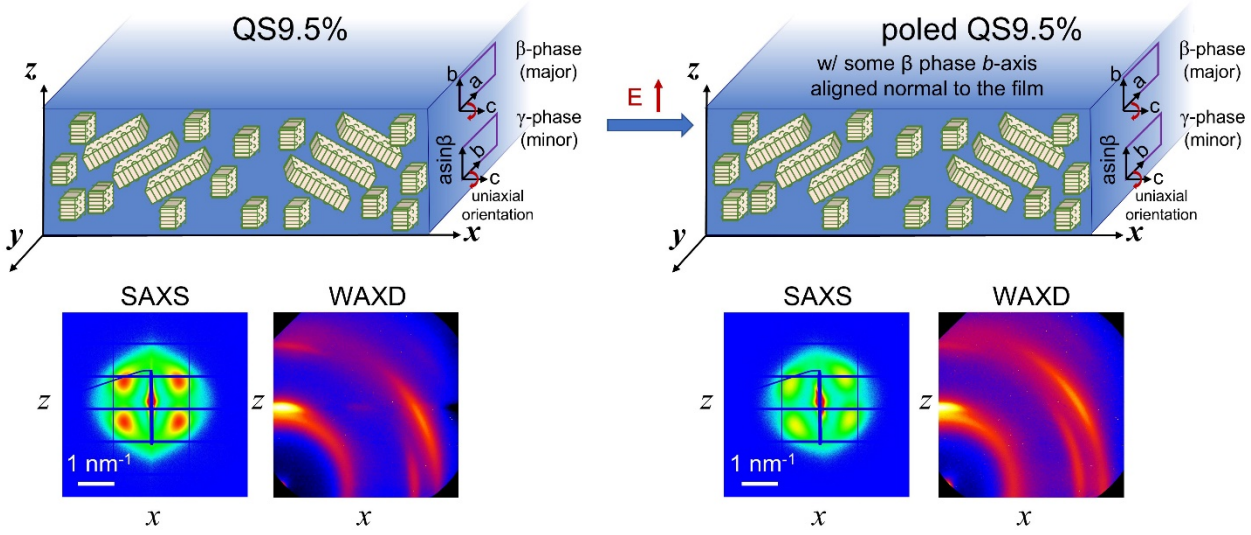

Figure S8. (Top panel) Schematic representation of QS9.5% before and after unipolar poling (200 MV/m at 10 Hz for 20 cycles). (Bottom panel) 2D SAXS and WAXD patterns for the QS9.5% films before and after unipolar poling. The *x*-direction is the stretching direction, the *z* direction is the film normal direction, and the *y* direction is the transverse direction. The X-ray beam was directed along the *y* direction.

Similar to QS4.4%, 2D SAXS and WAXD pattern for the QS9.5% sample before unipolar poling should be explained by the schematic representation in the top left panel in Figure S8. Basically, large tilted crystalline lamellae gave the butter-fly pattern in the 2D SAXS, and the small parallel crystallites gave the *c*-uniaxial oriented pattern in the 2D WAXD. The small crystallites

contained a major β phase and a minor γ phase. Upon unipolar poling (200 MV/m at 10 Hz for 20 cycles), the large crystalline lamellae still gave the butter-fly pattern in SAXS. In WAXD, still a uniaxial pattern along the *c*-axes was seen in the right panel of Figure S8. However, some small β crystals were oriented with their *b*-axes parallel to the film normal direction (i.e., out of the diffraction condition). As a result, the intensity of the β phase slightly decreased after electric poling (see Figure 8B in the main text).

8. Estimation of Crystallite Size using Scherrer Equation

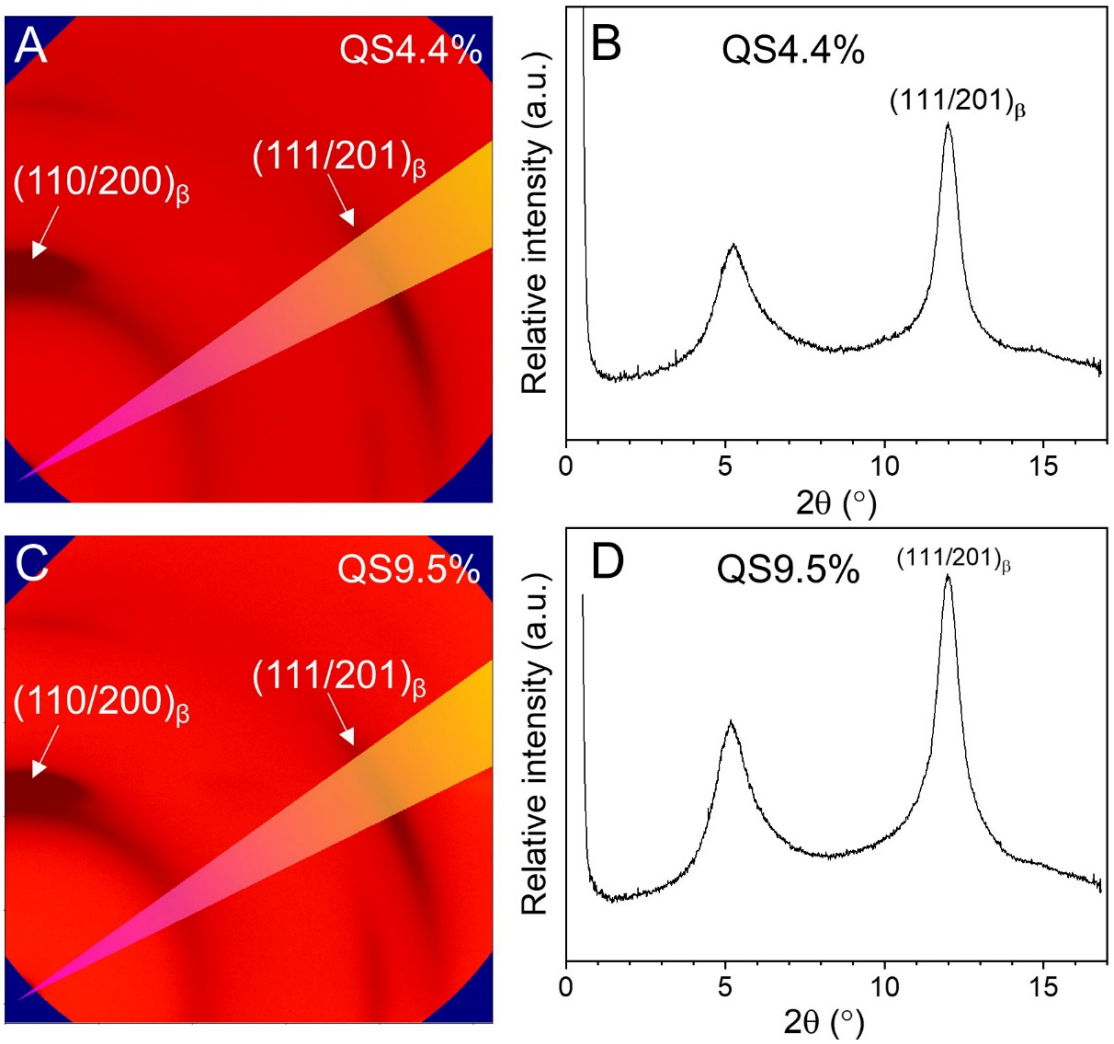

Figure S9. Estimation of crystallite sizes for (A,B) QS4.4% and (C,D) QS9.5% using the Scherrer equation; (A,C) 2D WAXD patterns and (B,D) 1D WAXD profiles obtained from the integration in the highlighted areas in the 2D patterns.

To estimate crystallite sizes of QS4.4% and QS9.5%, Scherrer equation is used:

$$\tau = \frac{K\lambda}{\beta \cos \theta_{hkl}} \qquad \text{(S1)}$$

where τ is the crystallite size for the (*hkl*) reflection, *K* is a constant vary between 0.89 and 1.39, and usually taken as 0.90 for PVDF, λ is the wavelength of the X-ray, β is the full width at half maximum (FWHM, in radians), and θ_{hkl} is half scattering angle. Note, the $(110/200)_\beta$ reflections were not chosen for the analysis, because they had significant overlap with several other reflections from the γ phase, i.e., $(110)_\gamma$, $(020)_\gamma$, and $(100)_\gamma$ reflections. Instead, the $(111/201)_\beta$ reflections were chosen because they did not overlap with other reflections (see Figures S9A/C). In addition, the instrument broadening around this *q* range could be estimated from the X-ray energy bandwidth, $dE/E = dq/q = 0.007$, corresponding to a FWHM of 0.086°. Obviously, this was ignorable as compared to the observed FWHM of 0.73° for the quenched and stretched samples. Finally, the estimated crystallite sizes were calculated to be 6.5 and 5.6 nm for QS4.4% and QS9.5%, respectively.

9. Bipolar D-E loops for QS4.4% and poled QS4.4%

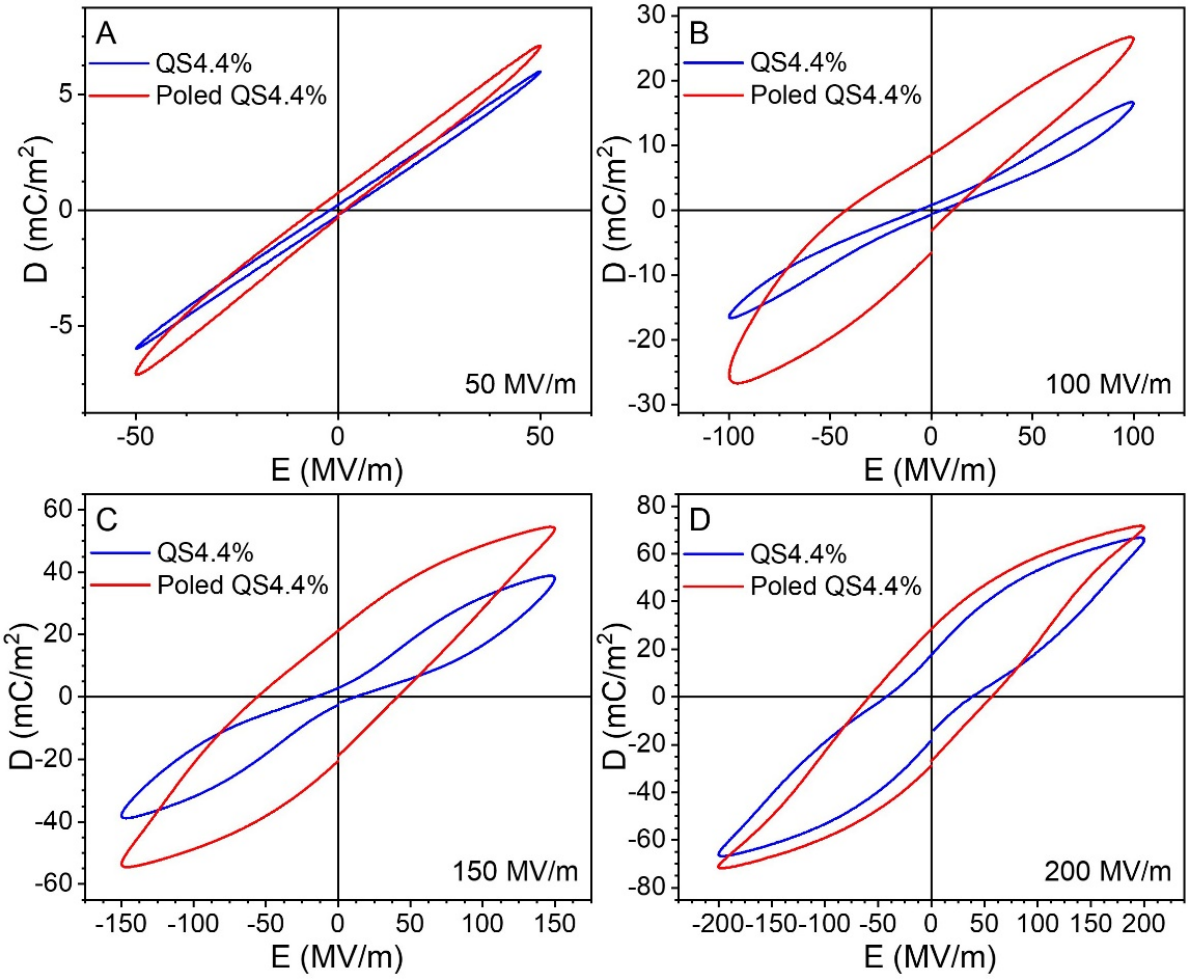

Figure S10. Bipolar D-E loops for the QS4.4% and the poled QS4.4% at (A) 50, (B) 100, (C) 150, and (D) 200 MV/m at room temperature. The poling frequency was 10 Hz with a sinusoidal waveform.

References

S1. Murasheva, Y. M.; Shashkov, A. S.; Galil-Ogly, F. A. Analysis of ^{19}F spectra of vinylidene fluoride-trifluorochloroethylene copolymers. *Polym. Sci. U.S.S.R.* **1980**, *21*, 968-974.